

NUMERICAL SIMULATION OF COMPOSITES GFRP-REINFORCED GLASS STRUCTURAL ELEMENTS UNDER MONOTONIC LOAD

Jorge Rocha^a, Eduardo Pereira^b, José Sena-Cruz^c, Luís Valarinho^d, João Ramôa Correia^e

ABSTRACT: Several reinforcing strategies have recently been developed to overcome glass brittleness and numerical simulations are essential to investigate the structural behaviour of such hybrid systems. Based on previous experimental results from monotonic quasi-static tests, this paper presents a numerical study about the flexural behaviour of glass beams reinforced with glass fibre reinforced polymer (GFRP) laminates bonded with two different adhesives: polyurethane and epoxy. The main objective of this study is to evaluate the efficiency of different constitutive models to simulate the non-linear behaviour of glass, considering the following factors: initial stiffness, cracking load, post-cracking stiffness, crack pattern and progressive failure. The glass is simulated using smeared crack (SCM) and damaged plasticity (DPM) models with static and dynamic numerical approaches. Particular attention is paid to the influence of the several parameters that influence the structural behaviour of glass (e.g. threshold angle), as well as to the interfaces between all the materials involved (e.g. thickness of the adhesive layer). In relation to static numerical approaches, dynamic numerical approaches require more computational effort and their dynamic effects may influence the structural responses obtained; however, they also show to be able to capture all the stages of cracking in greater detail, because stability during cracking formation is guaranteed even at smaller loading stages. Since DPM models do not allow considering a maximum absolute damage factor of 1.0, the smeared crack models simulate better the non-linear behaviour of glass.

^a PhD Student, ISISE, IB-S, University of Minho, School of Engineering, Campus de Azurém, 4800-058 Guimarães, Portugal. Email: a61858@alunos.uminho.pt

^b Assistant Professor, ISISE, IB-S, University of Minho, School of Engineering, Campus de Azurém, 4800-058 Guimarães, Portugal. Email: eduardo.pereira@civil.uminho.pt

^c Associate Professor, ISISE, IB-S, University of Minho, School of Engineering, Campus de Azurém, 4800-058 Guimarães, Portugal. Email: jsena@civil.uminho.pt

^d PhD Student, CERIS, Instituto Superior Técnico, Universidade de Lisboa, Lisboa, Portugal. Email: luís.valarinho@tecnico.ulisboa.pt

^e Full Professor, CERIS, Instituto Superior Técnico, Universidade de Lisboa, Av. Rovisco Pais, 1049-001, Lisboa, Portugal. Email: joao.ramoa.correia@tecnico.ulisboa.pt

21 **KEYWORDS:** Glass-GFRP composite beams; Numerical analysis; Smeared crack model; Damaged plasticity
22 model; Dynamic effects; Structural behaviour.
23

1. INTRODUCTION

Structural glass is nowadays of great relevance in contemporary architecture, due to its aesthetic and functional virtues [1, 2]. However, the structural behaviour of glass is substantially different from other building materials, such as steel and reinforced concrete [3]. The brittle behaviour of glass and the difficulties in anticipating its failure require the adoption of suitable safety measures.

To improve the structural performance of annealed glass, the industry has developed glass toughening to increase its tensile strength and glass lamination to overcome its brittleness [1,4] In the first method creates compressive stresses on outer surfaces, closing flaws and, therefore, increasing its tensile strength. However, the breakage of tempered glass creates smaller fragments, which reduces the residual strength. On the other hand, the second method consists of joining two or more glass sheets using an interlayer. The glass lamination prevents the failure of the entire element (redundancy) and, due to the interlayer action, the fragments will remain in place. The structural performance of laminated glass elements has been addressed in several experimental (e.g. [4]) and numerical (e.g. [5]) studies, evaluating the influence of different interlayers, loading conditions and temperatures. In order to improve the post-cracking performance of laminated glass with fully tempered glass plies, interlayers with embedded reinforcement have also been studied (e.g. [6]). However, the brittle behaviour of glass is not eliminated by either method.

In recent years, several reinforcing strategies have been developed to overcome glass brittleness [7], particularly the hybrid glass systems with timber (e.g. [8,9]), steel (e.g. [10–13]), Carbon Fibre Reinforcement Polymers, CFRP (e.g. [14,15]) and Glass Fibre Reinforcement Polymers, GFRP (e.g. [1,2,16–19]). Therefore, the selection of the type of adhesive to use is also critical, considering that there is a wide range of adhesives with different properties before and after hardening [20].

Numerical simulations are essential to investigate the structural behaviour of hybrid glass systems, or to design more complex or structurally demanding cases. However, the brittle behaviour of glass poses great challenges to the numerical simulations of structures comprising glass components, as well as the calibration of the material constitutive models adopted. Different authors have shown that the major challenges associated to the numerical simulation of structural glass behaviour, besides the calibration of the nonlinear constitutive models used for glass simulation, are (i) the realistic definition of the structural interaction between materials and (ii) the assessment of the post-cracking behaviour [19,21]. Several approaches have been used to study critical aspects related to laminated glass and/or hybrid glass structural elements: (i) the type of interlayer representation and

factors that influence its stiffness, such as temperature and load duration; (ii) the type of interaction between materials, mainly glass and reinforcement; and (iii) the type of constitutive models used to describe the non-linear behaviour of the glass and interlayer, as well as the behaviour of the reinforcement.

Different constitutive models suitable for representing brittle or quasi-brittle behaviour have been used to simulate the non-linear behaviour of glass. While Neto *et al.* [18] have used a discrete crack approach, Valarinho *et al.* [19], Bedon and Louter [21–24] and Louter *et al.* [25] have used a smeared crack approach. Damaged plasticity approach was also used by Bedon and Louter [26]. The numerical simulations in Bedon and Louter [21–24] were performed in the ABAQUS finite elements software, by employing the Rankine failure criterion for cracks detection. The “brittle failure” option was adopted to model cracking evolution in Bedon and Louter [21,22], while the “brittle shear” option was adopted in Bedon and Louter [23,24]. Finally, the study performed by Bedon and Louter [26] included the numerical simulation of post-tensioned glass beams using ABAQUS, by means of the “concrete damaged plasticity” model, commonly used for modelling concrete.

Because glass is an extremely fragile material, which has low fracture energy, some studies have adopted strategies to overcome problems related to the convergence of numerical models, such as linear sequential elastic analysis. The aim was to avoid a possibly negative tangential stiffness, which is the main cause for convergence problems found in non-linear analysis [25]. However, all these strategies require additional regularization procedures to obtain mesh objective results [18].

Considering the importance of developing accurate approaches for the simulation of glass structures, and the challenges that normally are associated to the simulation of the behaviour of brittle materials such as glass, this study is aimed at assessing the in-depth details associated to the numerical simulation of reinforced structural glass, including both the force-deflection response and the cracking evolution. This work presents a numerical study of the structural behaviour of glass beams reinforced with GFRP laminates, which were simulated using different Smeared Crack (SCM) and Damaged Plasticity (DPM) models, available in FEMIX [27] and ABAQUS 6.14 [28], as well as different static and dynamic numerical approaches. In order to evaluate the efficiency of these models for the simulation of the post-cracking behaviour, the different numerical responses were analysed and compared considering the following factors: initial stiffness, cracking load, post-cracking stiffness, crack pattern and progressive failure. For this purpose, the material parameters derived by Valarinho *et al.* [19], based on experimental tests of glass-GFRP composite beams, were used. In this context, the present work addresses two main novel aspects, (i) concerning the comparison of different approaches for the numerical simulation of reinforced structural glass, since existing literature is absent in such critical analysis; (ii) on the other hand,

literature often refers ABAQUS/Explicit analyses without addressing the influence of dynamic effects; both factors are critical for accurate simulations. The paper identifies the most critical factors and possible strategies to obtain quasi-static analysis without excessive computational effort.

2. TEST ON GLASS-GFRP COMPOSITE BEAMS

The numerical simulations of glass-GFRP composite beams were based on an exploratory experimental study carried out by Valarinho *et al.* [19]. These beams were tested following the four-point bending setup. The glass-GFRP composite beam specimens, as shown in Fig. 1, consisted of annealed glass panels, with cross section of 12×100 [mm], reinforced at the bottom face with a GFRP pultruded laminate with a cross section of 12×8 [mm]. These materials were joined using two different adhesives, with a 2.0 mm thick layer: (i) a polyurethane adhesive, Sikaflex 265, with low Young's modulus and considered as a flexible adhesive, and (ii) an epoxy adhesive, SikaDur 31-fc, with high Young's modulus and considered as a stiff adhesive.

Double-lap joint specimens were also tested in tension by Valarinho *et al.* [19], in order to characterize the bond behaviour between GFRP and glass. From these tests the following main conclusions were obtained: (i) in the specimens with flexible adhesive, which exhibited an initial linear behaviour, a significant loss of stiffness before collapse was observed (see Fig. 2(a)), with failure characterized by debonding at the glass-adhesive interface; (ii) the specimens with stiff adhesive exhibited a practically linear behaviour until the collapse (see Fig. 2(b)), eventually with glass failure.

Fig. 3 presents the structural behaviour of the glass-GFRP composite beams with polyurethane (*SFlex* beams) and epoxy (*SDur* beams) adhesives obtained from four-point bending tests [19]. These composite beams presented linear elastic behaviour until the first crack appeared in the glass panel. Due to the brittle nature of glass failure and the inherent variability of its tensile strength, the cracking loads reached during testing have shown some scatter, as well as the post-cracking responses. This variability is associated to the numerous flaws contained by glass, which are randomly distributed in the material – such flaws, which are very small in size (not distinguishable by the naked eye) result mainly from the production process, and also from cutting and handling operations [29]. This inherent characteristic of glass explains not only the relatively high scatter of its tensile strength (e.g. Veer and Rodichev [30]), but also the occurrence of relevant size effects [31]. In the post-crack phase, a progressive loss of stiffness was observed after the development of a single crack in the case of the glass-GFRP composite beams made with polyurethane adhesive (see Fig. 4(b)). In the case of the composite beams made

with epoxy adhesive, several cracks have developed, propagating towards the supports (see Fig. 4(a)). According to Valarinho *et al.* [19], the deflection increment before cracking (pre-cracking stage) ranged from 0.95 to 1.52 mm/min and then, during the post-cracking stage, between 1.70 and 3.21 mm/min. In these tests, both the applied load and the mid-span deflection were measured at an average acquisition frequency of 5 Hz. All glass-GFRP beams were tested at an average temperature of 24 °C and 60% of relative humidity.

The double-lap joint specimens have shown significant relative displacements between the glass pane and the GFRP laminate when flexible adhesives were used (about 20 times higher than for the stiff adhesives). For this reason, four strain gauges (SG1 to SG4) were installed at different locations of the *SFlex*-1 beam at its mid-span section: (i) SG1 was placed at the top edge of the glass panel; (ii) SG2 was placed at the bottom/bonded edge of the glass panel; (iii) SG3 was placed at the top/bonded edge of the GFRP laminate; and (iv) SG4 was placed at the bottom edge of the GFRP laminate. As depicted in Fig. 5, a significant slippage occurred at the bonded interfaces of *SFlex*-1, both before and after the first crack was formed. Therefore, Bernoulli's hypothesis was not observed for these beams.

3. NUMERICAL SIMULATION

Based on an initial estimation of the material nonlinear parameters derived in Valarinho *et al.* [19], different material models, based in smeared crack and damaged plasticity approaches, were studied to simulate the non-linear behaviour of glass, as detailed in the following sections.

3.1 Smeared crack approach

The smeared crack approach has been used by different researchers to describe the non-linear behaviour of brittle and quasi-brittle materials, e.g. concrete, masonry and glass. This approach can be categorized into fixed and rotating [32]. With the fixed concept, the orientation of the cracks is fixed during the entire computational process, whereas the rotating concept allows the orientation of the cracks to co-rotate with the axes of principal stress [32]. The multi-fixed crack concept provides an intermediate option.

The multi-fixed concept, used by FEMIX [27], is suitable for tension-shear conditions, which is typical of fracture propagation problems [32]. The cracks start only under tension conditions, in mode-I, and subsequently propagate in tension-shear conditions. In the described behaviour, the maximum principal stress directions rotate after crack formation, which leads to increasing discrepancy relatively to the fixed crack directions. After the first crack, a new crack may appear when: (i) the maximum principal stress of an integration point exceeds the defined

tensile strength, and (ii) the angle between the direction of the existing cracks and the direction of the maximum principal stress exceeds the value of a predefined threshold angle.

The smeared crack approach contributes to describe the structural behaviour of the material when the maximum principal stress exceeds the uniaxial tensile strength. The main assumptions of this numerical approach are: (i) the damaged area is distributed by a specific crack band width, h , and (ii) the constitutive law of the damaged material is characterized by a tension-softening diagram, which, together with the fracture energy, G_f , are considered as material properties [33]. The type of tension-softening diagram and the number of cracks in each integration point are parameters required by the multi-fixed smeared crack approach [34].

Bazant and Oh [33], Sena-Cruz [34] and Rots *et al.* [35] proposed different ways to estimate the crack band width: (i) equal to the square root of the area of the finite element, (ii) equal to the square root of the area of the integration point, and (iii) equal to a constant value. The mesh objectivity must be ensured by the relationship between the crack band width and mesh size [32,34]. According to de Borst [36], the computational instabilities and convergence problems (e.g. snap-back instabilities) are avoided when the Eq. (1) is fulfilled. Therefore, the crack band width must be controlled to guarantee the stability and convergence of the smeared crack models. The other parameters are assumed to be constant properties of the material. The minimum fracture energy required for a stable numerical process is given by Eq. (2), obtained from the manipulation of Eq. (1).

$$h \leq \frac{G_f E}{f_f^2 b} \quad (1)$$

$$G_f \geq \frac{f_f^2 b h}{E} \quad (2)$$

The smeared crack approach was formulated in such a way that not only tension-softening but also crack shear can be taken into account through the shear retention factor, β [35]. This can be defined in two different ways [32,34]: (i) a constant value, and (ii) a non-constant value using the Eq. (3), where p is a constant value (e.g. 1, 2 or 3), ϵ_n^{cr} and $\epsilon_{n,ult}^{cr}$ are the crack normal strain and the ultimate crack normal strain, respectively.

$$\beta = \left(1 - \frac{\epsilon_n^{cr}}{\epsilon_{n,ult}^{cr}} \right)^p \quad (3)$$

The constant shear retention factor implies a linear ascending relation between shear stress and shear strain across the crack, as well as a constant crack shear modulus [32]. In addition to the arbitrariness in choosing this value, the shear stress can increase indefinitely with a constant shear retention factor and, consequently, the maximum principal stress directions in cracked elements rotate ceaselessly [32].

The ABAQUS uses a smeared crack approach with fixed concept (orthogonal cracks). Therefore, the maximum number of cracks at an integration point is limited by the number of stress components, e.g. 3 cracks in 3D models and 2 cracks in 2D models. According to ABAQUS [28], although the fixed concept has the orthogonally limitation, it is considered superior to the rotating concept when the effect of multiple cracks is important, since the last concept is restricted to a single crack at each integration point. The shear retention factor is defined as a non-constant value through the Eq. (3).

3.2 FEMIX smeared crack model (SCM-FEMIX)

This Section presents the assumptions adopted in the numerical simulation of the glass, GFRP and adhesives for the simulation of the beams with the FEMIX software. Three different strategies were considered to simulate the adhesive joint of composite beams: (i) the *Perfect Bond (PB)* between the glass and GFRP laminate, neglecting the physical existence of the adhesive; (ii) the *Linear Elastic Behaviour (LEB)* of the adhesive, using plane stress elements for 2D models or solid elements for 3D models, and assuming perfect bond at the GFRP/adhesive and adhesive/glass interfaces; and (iii) the *Non-Linear Behaviour (NLB)* of the joint, using interface elements, simulating the non-linear behaviour of the interfaces (GFRP/adhesive and adhesive/glass) and the adhesive itself.

3.2.1 Annealed glass

According to the Guideline for European Structural Design of Glass Components [37], in the simulation the linear elastic behaviour of annealed glass a Young's modulus, E_g , of 70 GPa, a Poisson's ratio, ν_g , of 0.23 and a tensile strength, $f_{g,t}$, which ranges from 30 to 80 MPa, were adopted. In composite beams models, the glass was simulated by linear elastic behaviour in compression and in tension, before cracking. Rankine failure criterion was used for the crack detection. After the cracking, non-linear behaviour of the glass was simulated by the smeared crack model.

After a parametric study, in which the experimental and the numerical results were compared in terms of initial stiffness, cracking load, post-cracking stiffness, crack pattern and progressive failure of the composite beams, Valarinho *et al.* [19] defined the glass linear features required by this mechanical constitutive model. The

following properties were adopted: (i) tensile strength of 50 MPa, (ii) tension-softening diagram with linear shape, (iii) quadratic shear retention factor law, (iv) minimum mode-I fracture energy, G_g , to avoid snap-back instabilities, according to Eq.(2), and (v) crack band width equal to the square root of the finite elements area. A threshold angle of 30° was also defined for the development of new cracks, as well as the maximum number of two and three cracks in each element in 2D and 3D models, respectively.

3.2.2 GFRP

The GFRP was modelled as linear elastic material, for both compression and tension, assuming the following mechanical properties (obtained from tests): Young's modulus, E_{GFRP} , of 28.7 GPa, Poisson's ratio, ν_{GFRP} , of 0.28.

3.2.3 Interface

Based on the parametric study described in Valarinho *et al.* [19], where three strategies were tested for the numerical modelling of the adhesive bonded joint, the perfect bond (*PB*) strategy was adopted to simulate the composite beam with epoxy adhesive (stiff adhesive). Previous numerical simulations showed that the two alternative strategies (*PSE* and *NLB*) did not accurately capture the experimental response after cracking, in terms of stiffness and ultimate load.

The polyurethane adhesive of the *SFlex* beam was described by the non-linear behaviour (*NLB*) strategy using a non-linear bond-slip relationship, as suggested in Valarinho *et al.* [19]. The *PB* strategy was initially excluded because it neglected the physical existence of the adhesive layer. On the other hand, previous simulations using the *PSE* strategy showed higher post-cracking stiffness than the one observed in the experimental responses, since it was not able to simulate the adhesive failure. Assuming a bilinear bond-slip relationship, Table 1 presents the used properties: (i) the linear elastic tangential stiffness, K_t , (ii) the shear strength, τ_m , and (iii) the mode-II fracture energy, G_m . The linear elastic tangential stiffness was assumed to be the same in both directions of the adhesive layer. Finally, according to Sena-Cruz [34], a high value of the linear elastic normal stiffness, K_n , was adopted in order to avoid any influence on the shear behaviour of the interface elements.

The non-linear bond-slip relationship used in Valarinho *et al.* [19] is governed by the Eq. (4), where τ_m and s_m are the maximum shear stress and the corresponding maximum slip, respectively, and the shape of the pre- and post-peak curves are defined respectively by the parameters α and α' [34]. The mechanical properties used to

model the polyurethane adhesive are presented in Table 2. The mode-II fracture energy, G_m , was calculated as the integral of the post-peak curve, according to Eq. (5).

$$\tau(s) = \begin{cases} \tau_m \left(\frac{s}{s_m} \right)^a & \text{if } s \leq s_m \\ \tau_m \left(\frac{s}{s_m} \right)^{-\alpha'} & \text{if } s \geq s_m \end{cases} \quad (4)$$

$$G_m = \int_{s_m}^{\infty} \tau_m \left(\frac{s}{s_m} \right)^{-\alpha'} ds \quad (5)$$

3.2.4 Mesh strategy

Taking into account the real geometry and the symmetry conditions of the glass-GFRP composite beams (see Fig. 1), only half span was numerically simulated ($l = 700$ mm). In the *SDur* beams, 8-node plane stress elements, with 2×2 Gauss-Legendre integration scheme, were used to simulate the glass panel and GFRP laminate (2D models). However, to compare the results obtained in the three material models (reasons are given in Section 3.3.3), 20-node solid elements were also used to simulate the different structural materials (GFRP laminate and glass panel) of the *SFlex* beams (3D models).

In the *NLB* strategy, in agreement with the previously presented assumptions, the adhesive layer was simulated by 16-node interface elements with 3 (height) \times 2 (thickness) using Gauss-Lobatto integration rule. The thickness of the adhesive joint was reproduced by positioning the glass panel at a distance of 2 mm from the GFRP laminate, which was then filled by the interface elements.

Based on the sensitivity of mesh analysis carried out in Valarinho *et al.* [19], elements of 10×10 [mm] yield sufficiently accurate simulations. In the 3D models, only one layer of finite elements was used to describe the beam thickness (10 (width) \times 10 (height) \times 12 (thickness) [mm]). In order to avoid out-plane displacements, the z-direction displacements of the nodes located at the middle-thickness were prevented.

3.3 ABAQUS smeared crack model (SCM-ABAQUS)

As for the FEMIX smeared crack model (Section 3.2), similar assumptions and mechanical properties were adopted when using ABAQUS commercial package. The GFRP laminate was modelled as a linear elastic material with the same mechanical properties presented in Section 3.2.2. In the case of the simulation of the annealed glass, the smeared crack model available in ABAQUS/Explicit is suitable for quasi-static and dynamic analyses [28].

The computational effort required by ABAQUS/Explicit depends on the density of the materials [28]. Thus, a density of 2500 and 1600 kg/m³ was adopted for the annealed glass and GFRP, respectively. By default, ABAQUS/Explicit considers the geometric nonlinearity through the "NLgeom" setting. However, this option was ignored for the sake of simplicity because the influence of the geometric nonlinearity on the structural responses would be very small.

3.3.1 Annealed glass

The compressive behaviour of annealed glass was assumed as linear elastic. The brittle failure in tension was properly considered by adopting the "Brittle Cracking" mechanical model, using the "Brittle Shear" option to model crack evolution. This constitutive model is suitable for concrete brittle and quasi-brittle materials, and it was also adopted for glass [19,21–23,25,26]. Before the tensile strength is reached, the linear elastic behaviour was assumed.

In the "Brittle Cracking" model, a Rankine failure criterion is used for the crack detection. The main parameters introduced in this material model are: (i) the tensile strength, (ii) the mode-I fracture energy, and (iii) shear retention factor law (in "Brittle Shear" option). Similarly to the FEMIX models (Section 3.2), the following properties were adopted: tensile strength, $f_{t,g}$, of 50 MPa, minimum mode-I fracture energy, G_g , and quadratic shear retention law. The ABAQUS approach adopts, by default, a crack band width, h , equal to the square root of the finite elements area, as well as a linear tension-softening diagram when the "GFP" option (fracture energy cracking criterion) is selected [28]. Therefore, the maximum crack opening strain, ϵ_{max}^{ck} , required by the "Brittle Shear" option to define the quadratic shear retention law is given by Eq. (6), and was set to 8.0×10^{-4} .

$$\epsilon_{max}^{ck} = \frac{2G_g}{hf_{t,g}} \quad (6)$$

3.3.2 Interface

The *PB* and *NLB* strategies were used to simulate the *SDur* and *SFlex* beams, respectively. The interface GFRP/glass was modelled by adopting the "Surface-Based Cohesive Behaviour" with "Progressive Damage and Failure". This interface model is suitable for situations where the interface thickness is negligible [28], so the thickness of the adhesive layer was not considered in the simulations.

The constitutive model of the interface was described by the linear elastic normal stiffness, K_n , the linear elastic tangential stiffness in each direction of the adhesive layer, K_t , the normal strength, σ_m , the shear strength, τ_m , and the mode-II fracture energy, G_m , assuming a linear softening law. The interface material models used in FEMIX and ABAQUS were characterized by similar parameters, defined in Table 1.

3.3.3 Mesh strategy

Like in SCM-FEMIX, in these numerical models only half span of the composite beams was discretized. Considering the interface model adopted (see Section 3.3.2), ABAQUS/Explicit does not allow the edge-to-edge contact. Therefore, three-dimensional (3D) simulations of the *SFlex* beams was performed using 8-node solid elements with reduced integration (C3D8R).

On the other hand, 4-node plane stress elements with reduced integration (CPS4R) were used to simulate the *SDur* beams (2D models). The 2×2 integration scheme in 4-node elements is not supported by ABAQUS/Explicit, as well as 8-node elements with 3×3 or 2×2 integration schemes [28]. The adhesive layer was simulated by 4-node zero thickness surface elements (SFM3D4), with 4 integration points (surface-to-surface).

A mesh of 5 (width) \times 5 (height) [mm] finite elements was adopted for *SDur* beam, in order to maintain a consistent number of degrees of freedom with respect to SCM-FEMIX (see Section 3.3.4), where the finite elements were assigned with a 2×2 integration scheme. Two layers of finite elements of 10 (width) \times 10 (height) \times 6 (thickness) [mm] were used to describe the thickness of the *SFlex* beam. This approach was adopted in order to avoid out-plane displacements, and the z-direction displacements of the nodes located at the middle-thickness, which are shared by the two layers of finite elements that describe the thickness of the beam, were prevented. The adoption of finite elements of 5 (width) \times 5 (height) \times 6 (thickness) [mm] would require a high computational effort and, in the case of the *SFlex* beam, would not significantly improve the capturing of its post-cracking behaviour, as verified by preliminary simulations.

Linear elements (e.g. CPS4R and C2D8R) with reduced integration tend to be too flexible due to the hourglass problem. The distortions may be such that the deformations calculated at the integration point are all zero, leading to uncontrolled distortion of the mesh [28]. Hourglass is usually controlled by introducing counteracting internal nodal forces. The ABAQUS/Explicit provide five different hourglass controls: (i) relax stiffness (by default); (ii) enhanced; (iii) stiffness; (iv) viscous; and (v) combined (stiffness and viscous) [28]. According to Mostafawi [38], the viscous and combined hourglass controls give very large artificial energy and

are not appropriate for quasi-static problems. On the other hand, the enhanced hourglass control is not appropriate for nonlinear problems, since it provides increased resistance and may yield overly stiff responses [28]. In the present study the stiffness relax was adopted to control hourglass.

3.3.4 Dynamic effects

According to Chen *et al.* [39], (i) the loading time, (ii) the loading scheme, (iii) the damping ratio, (iv) the time increment size and (v) the time integration method are factors that affect the accuracy of quasi-static simulations with models that are intrinsically dynamic. The correct combination of these factors allows to reduce the dynamic effects of the models and obtain quasi-static responses. In ABAQUS, the viscous damping is defined as Rayleigh Damping, where the viscous damping matrix, C , is expressed as a linear combination of the mass matrix, M , and the stiffness matrix, K (see Eq.(7)). The damping ratio for the j^{th} mode of the system can be expressed by Eq. (8).

$$C = \alpha_0 M + \beta_0 K \quad (7)$$

$$\xi_j = \frac{\alpha_0}{2\omega_j} + \frac{\beta_0 \omega_j}{2} \quad (8)$$

The α_0 and β_0 parameters of Eqs. (7) and (8) are constants for mass and stiffness-proportional damping, respectively. On the other hand, ω_j is the angular frequency corresponding to the j^{th} mode. The period, T_1 , and the angular frequency, ω_1 , of the fundamental vibration mode of the *SDur* beams, which were determined using the "linear perturbation procedures" available in ABAQUS/Standard, are equal to 0.255 seconds and 24.63 rad/s, respectively. According to Chen *et al.* [39], the loading time should be in the range of $50T_1$ to $100T_1$ (14 to 28 seconds, approximately). As the *SFlex* beams have a lower stiffness than the *SDur* beams, since the polyurethane adhesive is flexible, a loading time of 17.5 and 12.5 seconds was used for the *SDur* and *SFlex* beams, respectively.

The application of loading induces large dynamic effects, due to the initial velocity and acceleration [39]. A linear loading scheme was adopted because, as the loading rate is constant during the process, the acceleration is null during most of the loading process and its influence on the structural response is negligible. The adoption of a smooth loading scheme in general requires longer loading time or, to complete the process within the

predefined time, a higher loading rate. However, the increase of these two parameters could increase the dynamic effects [39].

In ABAQUS/Explicit, by default, the time increment scheme is fully controlled by the stability limit of the central difference method and requires no user intervention, which would always adopt a non-optimized value [28]. Therefore, an automatic time increment size was used. According to ABAQUS/Explicit [28] a small damping is introduced to control high frequency oscillations. The maximum stable time increment with damping is given by the Eq.(9), where ξ_{max} is the ratio of critical damping of the vibration mode with the highest frequency (ω_{max}). In this way, the damping reduces the stable time increment and, consequently, increases the computational cost.

$$\Delta t \leq \frac{2}{\omega_{max}} \left(\sqrt{1 + \xi_{max}^2} - \xi_{max} \right) \quad (9)$$

Considering the numerical models presented in Chen *et al.* [39], the mass-proportional damping may become unstable and fail. On the other hand, to create the same level of critical damping in the lowest vibration mode, the stiffness-proportional damping requires more computational cost, since it causes a larger decrease in the maximum stable time. Thus, the mass-proportional damping, which has a higher damping efficiency for the low frequency vibration modes, was applied in this work.

According to ABAQUS [28], an approximation to the stability limit is given by the Eq.(10), where L_{min} is the smallest element dimension in the mesh and c_d is the dilatational wave speed, calculated from the Eq. (11), where ρ is the density. In an isotropic and elastic material (e.g. glass), the effective Lamé's constants $\hat{\lambda}$ and $\hat{\mu}$ can be computed based on the Young's Modulus, E , and Poisson's ratio, ν , using Eqs. (12) and (13), respectively.

$$\Delta t = \frac{L_{min}}{c_d} \quad (10)$$

$$c_d = \sqrt{\frac{\hat{\lambda} + 2\hat{\mu}}{\rho}} \quad (11)$$

$$\hat{\lambda} = \lambda_0 = \frac{E\nu}{(1+\nu)(1-2\nu)} \quad (12)$$

$$\hat{\mu} = \mu_0 = \frac{E\nu}{2(1+\nu)} \quad (13)$$

Analysing Eqs. (10), (11), (12) and (13), the computational effort can be reduced by increasing the material density, using the mass scaling, which reduces the dilatational wave speed, or increasing the dimensions of the finite elements. As all finite elements have the same dimensions, the last option was not adopted because it would decrease the number of degrees of freedom of the mesh.

3.4 ABAQUS damaged plasticity model (DPM-ABAQUS)

The assumptions and mechanical properties adopted in the previous models (see Section 3.3) were also used in case of the simulations with the Damaged Plasticity Model (*DPM*), mainly: (i) the GFRP was modelled as a linear elastic material (mechanical properties presented in Section 3.2.2); (ii) the *PB* and *NLB* strategies were used in *SDur* and *SFlex* beams, respectively; (iii) the "Surface-Based Cohesive Behaviour" with "Progressive Damage and Failure" were used to describe the interface GFRP/glass (mechanical properties presented in Table 1); and (iv) the finite elements CPS4R, C3D8R and SFM3D4 were used to simulate the *SDur* and *SFlex* beams. Although the *DPM* is available in ABAQUS/Standard, the simulations were performed in ABAQUS/Explicit for the sake of comparison and to avoid snap-back instabilities, mainly in the simulation of the *SFlex* beam that, comparing with *SDur* beam, has a more brittle behaviour.

As stated before, the glass was model with the "Concrete Damage Plasticity" model. This model was originally used in the simulation of reinforced concrete elements [40–42], and then extended to the simulation of other quasi-brittle materials, e.g., glass [26] and masonry. The inelastic compressive and tensile behaviours are described by multi-hardening plasticity and a scalar isotropic damaged elasticity, respectively [28]. Thereby, the definition of the yield surface and the plastic flow are required by DPM-ABAQUS through the following parameters: (i) the dilation angle, ψ ; (ii) the eccentricity, ϵ , which defines the shape of plastic flow; (iii) the ratio between the initial biaxial compressive yield stress, f_{bc} , and the initial uniaxial compressive yield stress, f_c ; and (iv) the shape of yield surface, defined by K_c . The dilation angle was set to 1°. According to the recommendations in ABAQUS [28] for quasi-brittle materials, such as concrete, values of 0.1, 2/3 and 1.16 were considered for ϵ , K_c and f_{bc}/f_c ratio, respectively.

The mechanical parameters required to simulate the tensile behaviour of glass are: (i) the yield stress, σ_t , (ii) the mode-I fracture energy, G_f , and (iii) the damage law, defined by the d_t parameter [28]. The minimum mode-I fracture energy was adopted to avoid snap-back instabilities, such as in the case of smeared crack models (see Sections 3.2 and 3.3). As mentioned in 3.3.1, when the GFI option is selected, the ABAQUS software assumes a

linear tension-softening diagram. Therefore, the maximum total displacement, u_{max} , which also includes the elastic deformation, was determined by Eq. (14) and its value is equal to 1.514×10^{-2} mm.

As glass has a brittle nature, the plastic strain, ε_t^{pl} , is essentially null ($\varepsilon_t^{el} = \varepsilon_t$). According to ABAQUS [28], an excessive damage factor may have a critical effect on the rate of convergence. A damage factor of 0.99 was assigned to the maximum total displacement, which corresponds to a 99% reduction of the stiffness, taking into account recommendations given in [28]. Based on these aspects, the damage law adopted is presented in Fig. 6, as well as the corresponding mechanical constitutive model.

$$u_{max} = \frac{hf_{t,g}}{E_g} + \frac{2G_g}{f_{t,g}} \quad (14)$$

3.5 Parametric study

The structural behaviour of glass composite systems can be divided in two stages, separated by the appearance of the first crack: the pre- and post-cracking stages. Initially, during the pre-cracking stage, glass behaves as a linear elastic material until the maximum principal stress exceeds its tensile strength, regardless of the numerical model adopted. Therefore, the pre-cracking response (e.g. stiffness and cracking load) is controlled only by elastic properties, such as Young's modulus and tensile strength. On the other hand, during the post-cracking stage, the behaviour of annealed glass is controlled by the constitutive models, through the material parameters required by each model to define the post-peak response (softening branch).

However, the input parameters required to define the cracked behaviour of glass involve higher uncertainty, either due to the difficulty of measuring these material properties in glass (e.g. fracture energy) or because these constitutive models were not specifically developed to simulate glass (e.g. DPM-ABAQUS). Thus, a parametric study was carried out concerning these input parameters, namely the threshold angle (β) in SCM-FEMIX, the fracture energy (G) in SCM-ABAQUS and DPM-ABAQUS and, finally, the dilation angle (ψ) and the shape of the yield surface (K) in DPM-ABAQUS. For the sake of simplicity, only *SDur* beams were considered for this parametric study, due to their extensive cracking during the post-cracking behaviour. The results will be presented and compared in Section 4.1.2, in terms of structural response and crack pattern.

As previously mentioned in Section 3.1, while a multi-fixed concept is used by SCM-FEMIX, SCM-ABAQUS uses, by default, a fixed concept (orthogonal cracks). At integration points close to the bottom edge of the glass panel, large rotations in their maximum principal stresses are expected due to the shear stresses induced by the GFRP/glass interface. Thereby, special attention was given to the influence of the threshold angle on the

post-cracking response of *SDur* beams. For this purpose, a threshold angle of 90° (fixed concept) was also considered in SCM-FEMIX, later called SCM-FEMIX- 90° .

As glass is extremely brittle, its fracture energy is close to zero. However, according to Eq. (2), a minimum mode-I fracture energy should be used to avoid numerical instabilities in static analysis, taking into account the mesh pattern and the mechanical properties of the material, that is, the tensile strength and the Young's modulus. In contrast, when adopting dynamic approaches, such as the one adopted by ABAQUS/Explicit [28], lower values than the minimum mode-I fracture energy can be used ensuring the convergence of models. In previous numerical studies on glass [21–24,26,43], a value of 3 J/m^2 (0.003 N/mm) [44] has been used to define the fracture energy of annealed glass, regardless of the mesh size. Therefore, this value was also considered in this parametric study.

On the other hand, the dilatancy is the physical phenomenon that describes the increase in volume of the material microstructure caused by shear stresses. This phenomenon is mainly associated with soils and quasi-brittle materials (heterogeneous materials). Compared to concrete, smooth surfaces are created when the glass breaks. Therefore, the dilation angle in glass is likely lower than in concrete, which is usually greater than 30° , according to Coronado and Lopez [41]. Values of 1° , 10° and 20° were considered.

As the *SDur* beams were numerically simulated neglecting the physical existence of the adhesive layer, according to *PB* strategy (see Section 3.2.3), considerable shear stresses were expected near the bottom edge of the glass panel. Thereby, the influence of the yield surface shape was considered in this parametric study. Values of 0.5 (Rankine yield surface), 0.67 (recommended value in ABAQUS [28]), and 1.0 (Von Mises yield surface) were considered for the crack detection criteria.

In addition to the material parameters required by the constitutive models, the post-cracking behaviour of glass-GFRP composite systems is influenced by the mesh pattern, which determines whether a numerical model is capable of capturing in detail all the failure processes that were observed experimentally. Thus, the ability to capture localized phenomena, such as the progressive detachment of the GFRP laminate towards the supports, can be substantially influenced by the mesh pattern adopted, both the mesh size and the number of integration points per finite element. In the present research 8-node plane stress elements of $10 \times 10 \text{ [mm]}$ with 2×2 Gauss-Legendre integration scheme were used in SCM-FEMIX, while 4-node plane stress elements of $5 \times 5 \text{ [mm]}$ with reduced integration (CPS4R) were used in ABAQUS models to simulate *SDur* beams. In order to assess the influence of the mesh pattern on each ABAQUS model, a sensitivity analysis was carried out considering two additional mesh sizes: 2.5×2.5 and $10 \times 10 \text{ [mm]}$.

4. RESULTS AND DISCUSSION

Figs. 7, 8 and 9 show the load (F) vs. deflection at mid-span (δ) responses of *SDur* and *SFlex* beams obtained from the numerical simulations, as well as the crack patterns obtained at relevant phases: (i) onset and end of the post-cracking stage of *SDur* beams, and (ii) after cracking for the *SFlex* beams. In *SDur* beams, the crack patterns are also presented at an intermediate stage of the post-cracking response to show the evolution of the cracking processes. The *SDur* beam analysis was stopped when the initial cracking load was fully recovered. On the other hand, in the simulation of *SFlex* beam, the analysis was stopped when the deflection of 12 mm was attained, since the post-cracking stage of these composite beams showed an almost linear steady recovery of the load carrying capacity. Additionally, the further computation was difficult due to pronounced numerical instabilities after this displacement was attained, most likely due to the large opening of the cracks already formed.

Fig. 10 shows the load vs. deflection responses obtained by using the three numerical models, as well as the experimental results obtained for the composite beams made with epoxy (*SDur*) and polyurethane (*SFlex*) adhesives (two test results are presented for each type of beam). Table 3 summarizes, for the simulated beams, the main parameters characterizing their structural behaviour: elastic stiffness, K_{el} , cracking load, F_{ck} , and corresponding deflection, u_{ck} .

4.1 *SDur* beams

4.1.1 Pre-cracking stage

In the pre-cracking stage, the assumptions of the *PB* strategy (perfect bond between the GFRP laminate and the glass) resulted in a slight difference between the numerical and the experimental stiffness of the response in the elastic domain, since the physical absence of the epoxy adhesive layer caused a small decrease in the section height (108 mm) and, consequently, in its flexural stiffness.

While the load vs. deflection curve obtained from the SCM-FEMIX (static analysis) remains perfectly linear during the pre-cracking stage, in the ABAQUS models this does not occur. The equation of motion of a dynamic structural problem is described by Eq. (15), where: (i) F is the applied external force; (ii) M , C and K are the mass, damping and stiffness matrix of the structural element, respectively; and (iii) d , \dot{d} and \ddot{d} are, respectively, the displacement, velocity and acceleration vectors.

$$F = M\ddot{d} + C\dot{d} + Kd \quad (15)$$

In order to evaluate the influence of the dynamic effects on the structural responses, Fig. 11 presents, step-by-step (0.05 seconds), the relationship between the slope of the tangent line of the load vs. deflection curves

obtained from the ABAQUS models and elastic stiffness derived from the SCM-FEMIX (1.566 kN/mm). This relation, later designated R_k , is represented against the mid-span deflection in Fig. 11. The dynamic effects (inertial forces) are clearly visible at the beginning of the load vs. deflection curves obtained from the ABAQUS models, as shown by the rapid growth observed in R_k . The small perturbations of R_k caused by the high frequency vibration modes could be avoided by adopting stiffness-proportional damping, but the computational effort of the numerical models would increase and its accuracy would not significantly improve, namely regarding the cracking load.

In all numerical models the same mechanical properties of the materials have been adopted, but R_k is generally less than 1.0 throughout the pre-cracking stage (see Fig. 11). This was expectable, because while the equation of motion of a static structural problem depends only on the displacement, in a dynamic structural problem it depends also on the velocity and acceleration, as defined by Eq. (15). The tangent line to the load vs. deflection curve obtained from the DMP-ABAQUS increases unexpectedly before cracking. In order to evaluate the influence of the dynamic effects in this artefact, Fig. 12 presents the ratio between the viscous energy, E_v , and work of the external forces, E_w , being the viscous energy the energy dissipated by damping mechanisms, including bulk viscosity damping and material damping. The E_v/E_w ratio shows that dynamic effects are not responsible for the oscillations in the R_k ratio of the DPM-ABAQUS.

The first crack appears in the central region of the beam between the loading points in all models, inside the pure bending area. Taking into account this information, for the *SDur* beams, which were modelled assuming the perfect bond between glass and GFRP laminate (*PB* strategy), the analytical cracking load, $F_{ck,a}$, is given by Eq. (16), where $I_y = 1.111 \times 10^6 \text{ mm}^4$ (homogenized cross section), $y_g = 56.285 \text{ mm}$, $x_l = 470 \text{ mm}$ and $h_{gfrp} = 8.0 \text{ mm}$. On the other hand, considering the elastic integration method and neglecting the shear effects, the analytical deflection at mid-span corresponding to the cracking load, u_{ck} , is provided by Eq.(17), where $x_2 = 230 \text{ mm}$ and $EI_y = 7.779 \times 10^{10} \text{ N.mm}^2$. In the numerical modelling the crack initiation occurs when the stress at the integration points located right above the bottom edge of the glass sheet reach the tensile strength. Table 4 shows the elastic properties of *SDur* beams, computed from Eqs. (16) and (17), considering the assumptions mentioned previously.

$$F_{ck,a} = \frac{2f_{t,g}I_y}{(y_g - h_{GFRP})x_l} \quad (16)$$

$$\delta_{ck,a} = \left(\frac{F_{ck,a}x_1}{4}x_2^2 - \frac{F_{ck,a}x_1x_2}{2}x_2 + \frac{F_{ck,a}}{12}x_1^3 - \left(\frac{F_{ck,a}x_1^2}{4} + \frac{F_{ck,a}x_1x_2}{2} \right)x_1 \right) / EI_y \quad (17)$$

In general, the numerical and analytical results have shown a good agreement. The small differences observed may be due to: (i) the analytical approach, which omits the shear deformation effects and, consequently, may slightly underestimate the vertical deformations; and (ii) the distance between the first integration point at which cracking occurs and the surface between the glass and the laminate, where cracking initiates. Additionally, the deflection immediately before and immediately after cracking, which should be approximately similar as captured by the numerical models, were observed to be different in the experimental responses. However, in this case this was probably due to the relatively low rate of the data acquisition system used during the experiments (mean value of 5 Hz) when compared to the very rapid development of cracking (not captured by the transducers readings), as well as the difficulty usually associated with the control of tests where abrupt losses of stiffness or load carrying capacity occur.

4.1.2 Post-cracking stage

Comparing the numerical and experimental results, it is generally observed that all the numerical models captured reasonably well the post-cracking behaviour of *SDur* beams. However, the final crack patterns of the three models show significant differences. The failure caused by the excessive damage on the bottom edge of the glass panel was satisfactorily represented by SCM-FEMIX, through the formation of several cracks at the glass/GFRP interface, starting at the loading points and propagating towards the supports. However, these cracks, which eventually lead to the laminate detachment, are not clearly visible in the case of ABAQUS models, resulting in higher stiffness of the load vs. deflection responses during the entire post-cracking stage when compared to SCM-FEMIX (see Fig. 10). The type of smeared crack approach may justify this difference. While the SCM-FEMIX uses a multi-fixed concept, with a maximum of two cracks in each integration point and a threshold angle of 30° (see Section 3.2.1), the SCM-ABAQUS uses, by default, a fixed crack concept (orthogonal cracks), which in general leads to a stiffer response.

As shown in Fig. 14, the smeared crack approach mainly influences the propagation of cracks and, consequently, the post-cracking behaviour. The final crack pattern of SCM-FEMIX-90° (see Fig. 13), with predominantly vertical and more distributed cracks, resembles better the SCM-ABAQUS crack patterns and the experimental results (see Fig. 4(a)). SCM-FEMIX 90° and SCM-ABAQUS correctly simulated the distribution of cracks between loading points, although they were unable to reproduce the increasing slope of the cracks towards the supports, as was the case with DPM-ABAQUS (see Fig. 9). Considering the higher stiffness of the epoxy

adhesive, the GFRP/glass interface induces high shear stresses in the integration points near the interface. Consequently, the maximum principal stresses experience large rotations. As result, SCM-FEMIX 90° shows higher post-cracking stiffness than SCM-FEMIX.

Fig. 15 presents the structural response and the final crack pattern obtained from different mesh patterns (see Section 3.5). Like in SCM-FEMIX, SCM-ABAQUS with a fine mesh was able to capture the cracking at the GFRP/glass interface towards the support, resulting in lower stiffness during the post-cracking stage compared to the models with coarse meshes (5×5 and 10×10 [mm]). Therefore, the post-cracking behaviour of *SDur* beams obtained from SCM-ABAQUS is mesh dependent. According to ABAQUS [28], the smeared crack models inherently induce mesh sensitivity in the results. In opposition to SCM-FEMIX, SCM-ABAQUS requires an extremely fine mesh to obtain similar post-cracking behaviour, due to the lower sensitivity of the finite elements with reduced integration and the fixed smeared crack approach (orthogonal cracks). On the other hand, unlike SCM-ABAQUS, similar post-cracking responses were obtained from DPM-ABAQUS with different mesh patterns. As the maximum damage factor recommended by ABAQUS is 0.99 (see Section 3.4), all cracks retained a residual stress roughly corresponding to 1.0% of the glass's tensile strength. However, regardless of that, DPM-ABAQUS was unable to capture the cracking at the GFRP/glass interface, possibly due to the limitations previously discussed, which are inherent to the constitutive model adopted.

While in DPM-ABAQUS the cracked behaviour of glass is simulated through the progressive loss of material stiffness, in SCM-ABAQUS the cracked behaviour of glass is divided into two components: (i) the elastic deformation of un-cracked material and (ii) the contribution of cracking. According to Jirásek [45], stiffness degradation modeling can be considered only as a first approximation when the damage derives from the initiation and propagation of micro-cracks, since the damage models are more appropriate to simulate materials weakened by micro-voids (e.g. concrete). Regarding the crack pattern, the shear cracks experimentally observed (see Fig. 4(a)) were captured by DPM-ABAQUS, unlike SCM-ABAQUS.

According to Fig. 16, when the fracture energy of 3 J/m^2 was considered, SCM-ABAQUS was able to capture the cracking at the GFRP/glass interface, in agreement with the SCM-FEMIX results, providing lower post-cracking stiffness in relation to the model with the minimum fracture energy and, in turn, better resembling the experimental results. Considering the numerical simulations previously performed by Valarinho *et al.* [19] using SCM-FEMIX, the absolutely accurate definition of fracture energy was not essential to capture the post-cracking behaviour with precision. However, due to the dynamic nature of ABAQUS/Explicit, the more suddenly

the glass breaks (less fracture energy), the greater the dynamic effects which, in turn, influence the crack propagation and the structural response. In static analyses, like SCM-FEMIX, an extremely refined mesh of 0.15×0.15 [mm] would be required to avoid convergence problems in the model with fracture energy of 3 J/m^2 , since the minimum mode-I fracture energy depends on the tensile strength and Young's modulus of the material. Therefore, only in ABAQUS/Explicit it is possible to use a fracture energy lower than the minimum value given by Eq. (2), due to its dynamic nature.

On the other hand, the DPM-ABAQUS model with fracture energy of 3 J/m^2 provided a worse response than the model with the minimum mode-I fracture energy given by Eq. (2), both in terms of post-cracking behaviour and in terms of crack pattern. As mentioned in Section 3.4, DPM-ABAQUS is suitable to simulate concrete and other quasi-brittle materials. Therefore, although the ABAQUS/Explicit dynamic approach was used, DPM-ABAQUS showed difficulties to simulate materials with low fracture energy, like glass, resulting in crack patterns significantly different from those obtained experimentally. As shown in Fig. 16, when the lower fracture energy was used, the glass broke so suddenly that the zone comprised by the loading points was completely cracked. Thus, like in SCM-FEMIX, the minimum mode-I fracture energy given by Eq. (2) must also be used in DPM-ABAQUS. In addition, to avoid convergence problems during the analysis, a substantially longer loading time was required by the model with a fracture energy of 3 J/m^2 , thereby increasing the associated computational cost.

As shown in Fig. 17, the post-cracking behaviour of *SDur* beams is not influenced by the dilation angle. As dilatancy describes the increase in material volume caused by shear stresses, the dilation angle would only significantly influence the post-cracking behaviour if the crack propagation was dominated by mode-II (shear stresses). Although the mixed-mode-I+II occurred close to the GFRP/glass interface, due to the shear stresses induced by the reinforcement, the crack propagation was mainly controlled by mode I fracture (tensile stresses). On the other hand, irrelevant differences were also found between the models in terms of crack pattern, namely the bottom edge of the glass panel, although more distributed vertical cracks have been obtained with a dilation angle of 1° , better resembling to the experimental crack pattern. However, to ensure the convergence of the numerical models with larger values of the dilation angle, longer loading times were required, increasing in turn the computational cost. Furthermore, according to Malm [46], for dilation angles close to 0° , the material's behaviour is brittle, like glass, while for values close to the friction angle, the material's behaviour is ductile.

Regarding the shape of the yield surface, no significant differences are observed between the results provided by the distinct models (see Fig. 18), both in terms of post-cracking behaviour and crack pattern. When

the crack initiation is controlled by mode-I (tensile behavior), which is typical of brittle materials, the shape of the yield surface does not influence the material behavior.

4.1.3 Dynamic effects

The dynamic effects in ABAQUS/Explicit can be evaluated by comparing the kinetic energy, E_k , and internal energy, E_t [28]. Fig. 19 shows the E_k/E_t ratio for SCM-ABAQUS and DPM-ABAQUS during the entire numerical responses obtained. The E_k/E_t ratio should typically be less than 10% in quasi-static analyses [28]. At the beginning of the pre-cracking stage there is a kinetic energy peak (inertial forces), but during the remaining numerical response it is negligible, including during the entire post-cracking stage.

4.2 SFlex beams

4.2.1 Pre-cracking stage

As shown in Fig. 10, during the pre-cracking stage, a slight difference was obtained between experimental and numerical elastic stiffness. This difference may have been due to some discrepancies between the material parameters used to define the models and the real material parameters, as well as, although less likely, to the inherent experimental uncertainty, given that the displacements are small and the test is fast at this stage. Fig. 20 presents the crack pattern and numerical response of SCM-FEMIX-A, which is compared with the previously obtained numerical responses in Fig. 21. The elastic stiffness of the SFlex beam is slightly higher when the thickness of the adhesive joint is not simulated, SCM-FEMIX-A (1.393 kN/mm). As the polyurethane adhesive is more flexible, during the pre-cracking stage the behaviour of the SFlex beam is influenced mainly by the glass panel (approximately 90% of the total beam cross section). Therefore, the effect of neglecting the adhesive thickness on the numerical response is not significant.

Fig. 22 presents the $R_k - R_\delta$ relationship for each numerical model: R_k is the ratio between the slope of the responses obtained from SCM- and DPM-ABAQUS, calculated step-by-step (0.25 seconds), and the elastic stiffness derived from the SCM-FEMIX (constant value of 1.384 kN/mm), while R_δ is the ratio between the deflection during the pre-cracking stage and the deflection when the first crack occurred. Regarding the ABAQUS models, the SFlex beams showed to be more susceptible to high frequency vibration modes than the SDur beams, probably due to the three-dimensional simulation and to the explicit simulation of the adhesive joint (flexible).

This could be mitigated adopting a higher stiffness-proportional damping, but the computational effort of the numerical models would increase.

SCM-ABAQUS and DPM-ABAQUS show higher cracking loads than SCM-FEMIX (see Table 3). In addition to neglecting the adhesive joint thickness, in the case of both ABAQUS models the integration scheme used may also explain this difference. As Fig. 22 shows, neglecting the adhesive joint thickness has marginal influence on the cracking load.

Similarly to what was observed for *SDur* beams, also for the tests of the *SFlex* beams there seems to be a displacement jump right after cracking, which is probably due to the relatively low acquisition rate considering the velocity of the process involved, as well as the difficulty in controlling tests where abrupt losses of stiffness or load carrying capacity occur.

4.2.2 Post-cracking stage

All three numerical responses obtained are essentially similar when the post-cracking stage is considered. However, while the ABAQUS models show only a single vertical crack in the final crack patterns, SCM-FEMIX shows two cracks (see Figs. 7, 8 and 9). Besides the smaller sensitivity of the finite elements of the ABAQUS models, this difference can also be explained by the smeared crack approach used by each mechanical constitutive model, similarly to what was observed in the *SDur* beams. A multi-fixed concept with a maximum number of three cracks at each integration point and a threshold angle of 30° was used by the SCM-FEMIX, while the SCM-ABAQUS uses, by default, a fixed concept (orthogonal cracks), with a maximum number of three cracks at each integration point (3D models) and a threshold angle of 90° . The SCM-FEMIX-A- 90° (see Figs. 23 and 24) corresponds to the structural response of SCM-FEMIX with interface elements of zero thickness and a threshold angle fixed at 90° .

Unlike the epoxy adhesive, the polyurethane adhesive induces low shear stresses at the integration points above the bottom edge of the glass panel. Therefore, after the first crack, the maximum principal stresses experience small rotations in relation to the initial direction of the crack. As the polyurethane adhesive allowed the GFRP reinforcement to slip due to its flexibility, the formation of a failure mechanism at the bottom edge of the glass panel that could cause the detachment of the GFRP laminate did not occur in the *SFlex* beams. In this way, although the threshold angle seems to have influenced the crack pattern of the *SFlex* beams, especially in relation to the appearance of a second crack, it has negligibly influenced the post-cracking load-deflection numerical response of the *SFlex* beams.

The slightly higher post-cracking load obtained in DPM-ABAQUS may result from a slightly higher residual stress in the crack response, which is a consequence of the difficulty that plasticity models experience when dealing with strong localization of deformations, such as cracks. Additionally, the DPM-ABAQUS was not assigned with an absolute damage factor of 1.0 at the maximum crack opening displacement, as mentioned in Section 3.4, retaining in the crack a residual stress of 1.0% of the tensile strength of glass.

Table 5 compares the strain gauge measurements for the *SFlex*-1 beam with the values obtained from the three numerical models. Fig. 25 shows the experimental and numerical axial strain distributions along the mid-span cross-section of that beam at the crack initiation load (F_{ck}) and at the ultimate load (F_{ul}).

In general, the numerical models captured well the distribution of axial strains for F_{ck} , with relatively low differences between numerical and experimental results. Moreover, the significant slippage at the bonded interface was properly captured by the three numerical models. This provides further validation of the numerical models, namely of the constitutive model used to simulate the bond behaviour of the adhesive layer (*NLB* strategy), as well as of the elastic properties of the glass and GFRP laminate.

When F_{ul} is approached, in general the evolution of the axial strains observed in the numerical models resemble well the ones measured at the mid-span section of the *SFlex*-1 beam (see Fig. 25(b)). All numerical models seem to indicate that the GFRP laminate is mostly subjected to an almost constant axial strain along the thickness, with the exception of the section where the crack localizes. The experimental measurements show that besides a predominant extension deformation of the laminate (constant strain throughout the thickness), there is also a visible rotation component (see SG3 and SG4), suggesting that in the experiments a crack occurred in the vicinity of the mid-span section, where the strain gauges are located, and caused this localized bending effect on the laminate. Additionally, the measured axial strain at the bottom edge of the glass panel (SG2) for F_{ul} is approximately zero (see Fig. 25(b)), which is the likely result of the stress release caused by the formation of a nearby crack. Furthermore, the low interaction between the GFRP reinforcement and the glass substrate as a result of the low stiffness of the adhesive promoted large crack opening displacements that, in turn, induced a significant rotation effect on the GFRP laminate close to the cracked section (see Fig. 26), leading to compressive stresses at the top edge of the GFRP laminate and tensile stresses at its bottom edge. Nevertheless, the GFRP average axial strain obtained from the numerical model is quite close to the experimental one (1.61‰), providing further validation to the numerical models. On the other hand, the crack branching observed experimentally (see Fig. 4(b)) was not captured entirely by the numerical models. This resulted in a slight increase of the simulated flexural

stiffness of the *SFlex* beams, which in turn reduced the flexural stresses in the GFRP laminate. The numerical models presented some difficulty in capturing all features of the crack branching, which seems to have resulted in a stiffer numerical behaviour and in slightly higher ultimate loads (F_{ul}) compared to the experimental data.

4.2.3 Dynamic effects

Fig. 27 shows the E_k/E_t ratio (kinetic energy/internal energy) for SCM-ABAQUS and DPM-ABAQUS together with the numerical load-deflection responses. As mentioned in Section 4.1.3, the E_k/E_t ratio should typically be less than 10% in quasi-static analyses [28]. At the beginning of the pre-cracking stage a kinetic energy peak occurs, but after cracking the dynamic effects on the structural response are not significant. The damping introduced was sufficient to mitigate the dynamic effects during cracking, although the *SFlex* beams are very brittle. The kinetic energy reached high values at the beginning of the pre-cracking stage, exceeding the limit of 10% suggested in ABAQUS [28]. This could be avoided by adopting a smooth loading scheme, as mentioned in Section 3.3.4, but this would require a longer loading time or greater loading speed during the post-cracking stage to complete the process within the predefined time (12.5 seconds). A longer loading time would increase the computational cost (hours), while a greater loading speed during the post-cracking stage would compromise the convergence of the numerical models. Despite the peak kinetic energy at the beginning of the pre-cracking stage, the analyses are quasi-static, since this phenomenon occurred during a very short period and was immediately mitigated by the damping introduced in the model.

5. CONCLUSIONS

In this paper, an extensive numerical study was carried out in order to assess the performance of the constitutive models currently available to simulate the behaviour of glass structural elements reinforced with GFRP, in particular the smeared crack and the damaged plasticity models. For this purpose the experimental results obtained in a previous study were considered, that involved four-point bending tests of glass beams reinforced with GFRP laminates adhesively bonded with two different adhesives: polyurethane (*SFlex* beams) and epoxy (*SDur* beams).

The main conclusions may be summarized as follows:

- All mechanical constitutive models showed to be suitable to conveniently simulate the non-linear behaviour of glass structural beams. The cracking patterns formed and the progressive loss of stiffness observed in the experiments were correctly captured by the numerical models, particularly in the case of the *SFlex* beams, which have an extremely brittle behaviour. The different material models adopted have

been essentially influenced by a common set of non-linear parameters: tensile strength, mode-I fracture energy, shape of the tension-softening diagram, and type of shear retention factor, which, in the case of the Damaged Plasticity Model, was replaced by the damage evolution law.

- When compared to SCM-FEMIX, the computational effort required by ABAQUS models was very high, especially in the case of the 3D models of *SFlex* beams. The ABAQUS/Explicit, which is a dynamic-based numerical approach, can also be used for quasi-static analysis by properly prescribing the loading time, the mass scaling factor, the loading scheme and, especially, the damping ratio. Although the damping ratio reduces the undesirable dynamic effects of the structural responses, its influence on the results obtained requires special attention. Considering the brittle nature of glass, the damping ratio is a numerical parameter that is very difficult to calibrate by experimental means.
- SCM-FEMIX results were more accurate mostly due to the absence of dynamic effects related to the loading time, the damping ratio and others. As a result, during the pre-cracking stages of *SDur* beams, SCM-FEMIX did not show the same non-linearity of the numerical responses obtained from ABAQUS models. In different situations these dynamic effects can result in the under or overestimation of the cracking loads of the ABAQUS models.
- The Damaged Plasticity Model is suitable for simulating the non-linear behaviour of glass structural elements. In comparison to the Smeared Crack Models (SCM), the structural responses obtained also represented well the post-cracking stage of glass-GFRP composite beams. However, the damaged plasticity model does not allow considering a maximum absolute damage factor of 1.0, which limits the reduction of the initial elastic stiffness to a maximum of 99%. Therefore, the effects of these residual stresses are present in the post-cracking response and they were mostly visible in the *SFlex* beams.
- The numerical models performed in ABAQUS/Explicit, of a dynamic nature, showed to be able to capture in greater detail all stages of the effects of cracking on the structural responses because, as opposed to FEMIX models, much smaller load steps are easily implemented and this results in better stability during crack formation.
- In the case of *SDur* beams, unlike the *SFlex* beams, the threshold angle showed to have a greater influence on the structural response throughout the entire post-crack stage, mostly regarding the crack patterns obtained. A threshold angle of 90° (ABAQUS models) seems to provide crack patterns which are more similar to experimental results at the initial stages of cracking. However, as cracking progresses, the

difficulties in simulating the rotation of the principal directions become evident. The multi-fixed crack approach (SCM-FEMIX) becomes more efficient in describing the progress of the cracking in the lower part of the beam towards the supports, which ultimately leads to failure by detachment of the GFRP reinforcement.

- In SCM-ABAQUS, refined meshes should be used to capture localized phenomena (e.g. cracking at the GFRP/Glass interface) which, due to the lower sensitivity of finite elements with reduced integration and the threshold angle of 90° (fixed concept), showed not to be fully captured by medium or coarse meshes. Due to the assumptions inherent to the constitutive model, DPM-ABAQUS showed difficulties in capturing the cracking processes at the GFRP/Glass interface in *SDur* beams, regardless of the mesh size.
- The minimum mode-I fracture energy should be used in opposition to values referred in literature, since convergence problems (e.g. snap-back instabilities) were avoided in SCM-FEMIX and, in DPM-ABAQUS, structural responses and crack patterns resemble better the experimental ones. In SCM-ABAQUS, models with fracture energy below the minimum value and medium size meshes seemed to provide responses and crack patterns similar to the ones obtained with the models with minimum fracture energy and fine meshes. However, also in SCM-ABAQUS, at least the minimum mode-I fracture energy must be used, because the lower the fracture energy, the greater the deleterious dynamic effects. In addition, if the dynamic effects excessively influence the crack propagation, better results can be obtained by changing either the loading scheme or the loading time.

For quasi-static analysis, both ABAQUS material models showed to be suitable to simulate the non-linear behaviour of glass. In addition, these constitutive models provided better stability during crack propagation in relation to SCM-FEMIX, allowing to capture cracking in more detail by adopting small loading steps. However, the ABAQUS material models showed the following limitations: (i) the finite elements with reduced integration required by ABAQUS/Explicit, which implies the adoption of fine mesh patterns to capture localized phenomena (e.g. cracking at the GFRP/glass interface); (ii) the fixed crack approach used by default, which reduces the sensibility of finite elements close to the reinforcement; and (iii) the maximum damage factor of 0.99 allowed by DPM-ABAQUS, which leads to the retention of residual stress in cracks corresponding to 1% of the glass's tensile strength.”

The numerical simulations carried out showed that the post-cracking behaviour of *SFlex* beams have less sensitivity to the mesh pattern and to the smeared crack approach, since one single vertical crack constitutes the crack pattern and the shear stresses at the GFRP/glass interface are negligible. Thus, the structural behaviour of

glass-GFRP composite systems with flexible adhesives are mainly influenced by the tensile strength of glass and the interface model used to simulate the adhesive layer. On the other hand, in *SDur* beams, where higher shear stresses at the GFRP/glass interface develop, the smeared crack approach and, mainly, the mesh pattern have a greater influence on structural responses.

ACKNOWLEDGEMENTS

The first and third authors wish also to acknowledge the grants SFRH/BD/122428/2016 and SFRH/BSAB/150266/2019, respectively, provided by Fundação para a Ciência e a Tecnologia, IP (FCT), financed by European Social Fund and by national funds through the FCT/MCTES.

REFERENCES

- [1] Correia J, Valarinho L, Branco F. Post-cracking strength and ductility of glass-GFRP composite beams. *Compos Struct* 2011;93:2299–309.
- [2] Valarinho L, Correia J, Branco F. Experimental study on the flexural behaviour of multi-span transparent glass-GFRP composite beams. *Constr Build Mater* 2013;49:1041–53. <https://doi.org/10.1016/j.conbuildmat.2012.11.024>.
- [3] Balan B, Achintha M. Experimental and Numerical Investigation of Float Glass-GFRP Hybrid Beams. In: Belis, Bos, Louter, editors. *Challenging Glas. 5 - Conf. Archit. Struct. Appl. Glas.*, vol. 97, Ghent: 2016, p. 281–96. <https://doi.org/10.2514/6.2009-5462>.
- [4] Biolzi L, Orlando M, Piscitelli LR, Spinelli P. Static and dynamic response of progressively damaged ionoplast laminated glass beams. *Compos Struct* 2016;157:337–47. <https://doi.org/10.1016/j.compstruct.2016.09.004>.
- [5] Yuan Y, Tan PJ, Li Y. Dynamic structural response of laminated glass panels to blast loading. *Compos Struct* 2017;182:579–89. <https://doi.org/10.1016/j.compstruct.2017.09.028>.
- [6] Biolzi L, Cattaneo S, Orlando M, Piscitelli LR, Spinelli P. Post-failure behavior of laminated glass beams using different interlayers. *Compos Struct* 2018;202:578–89. <https://doi.org/10.1016/j.compstruct.2018.03.009>.
- [7] Martens K, Caspeelee R, Belis J. Development of composite glass beams - A review. *Eng Struct* 2015;101:1–15. <https://doi.org/10.1016/j.engstruct.2015.07.006>.
- [8] Cruz P, Pequeno J. Structural Timber-Glass Adhesive Bonding. *Challenging Glas.*, 2008, p. 205–14.
- [9] Cruz P, Pequeno J. Timber-Glass Composite Beams: Mechanical Behaviour & Architectural Solutions. *Challenging Glas.*, 2008, p. 439–48.
- [10] Belis J, Callewaert D, Delincé D, Impe R Van. Experimental failure investigation of a hybrid glass / steel beam. *Eng Fail Anal* 2009;16:1163–73. <https://doi.org/10.1016/j.engfailanal.2008.07.011>.
- [11] Bos F, Veer F, Hobbelman G, Louter P. Stainless steel reinforced and post-tensioned glass beams. *ICEM12- 12th Int. Conf. Exp. Mech.*, Bari, Italy: 2004, p. 1–9.
- [12] Louter C, Belis J, Veer F, Lebet J. Structural response of SG-laminated reinforced glass beams; experimental investigations on the effects of glass type, reinforcement percentage and beam size. *Eng Struct* 2012;36:292–301. <https://doi.org/10.1016/j.engstruct.2011.12.016>.
- [13] Louter C, Cupac J, Lebet J. Exploratory experimental investigations on post-tensioned structural glass beams. *J Facade Des Eng* 2014;2:3–18. <https://doi.org/10.3233/FDE-130012>.
- [14] Louter C, Cupac J, Debonnaire M. Structural glass beams prestressed by externally bonded tendons. *Glas. Glob. Conf. Proc.*, Philadelphia, EUA: GlassCon Global; 2014, p. 450–9.
- [15] Palumbo M. A New Roof for the XIIIth Century 'Loggia de Vicari' (Arquà Petrarca – PD Italy) Based on Structural Glass Trusses: A Case Study. *Glas. Process. Days*, Tampere, Finland: 2005.
- [16] Achintha M, Balan B. Characterisation of the mechanical behaviour of annealed glass – GFRP hybrid beams. *Constr Build Mater* 2017;147:174–84. <https://doi.org/10.1016/j.conbuildmat.2017.04.086>.

- 777 [17] Bedon C, Louter C. Numerical investigation on structural glass beams with GFRP-embedded rods,
778 including effects of pre-stress. *Compos Struct* 2018;184:650–61.
779 <https://doi.org/10.1016/j.compstruct.2017.10.027>.
- 780 [18] Neto P, Alfaiate J, Valarinho L, Correia J, Branco F, Vinagre J. Glass beams reinforced with GFRP
781 laminates: Experimental tests and numerical modelling using a discrete strong discontinuity approach. *Eng*
782 *Struct* 2015;99:253–63. <https://doi.org/10.1016/j.engstruct.2015.04.002>.
- 783 [19] Valarinho L, Sena-Cruz J, Correia J, Branco F. Numerical simulation of the flexural behaviour of
784 composite glass-GFRP beams using smeared crack models. *Compos Part B Eng* 2017;110:336–50.
785 <https://doi.org/10.1016/j.compositesb.2016.10.035>.
- 786 [20] Pye A, Ledbetter S. The selection of an adhesive for the construction of a glass-adhesive T-beam. *Int J*
787 *Adhes Adhes* 1998;18:159–65. [https://doi.org/10.1016/S0143-7496\(98\)00055-4](https://doi.org/10.1016/S0143-7496(98)00055-4).
- 788 [21] Bedon C, Louter C. Exploratory numerical analysis of SG-laminated reinforced glass beam experiments.
789 *Eng Struct* 2014;75:457–68. <https://doi.org/10.1016/j.engstruct.2014.06.022>.
- 790 [22] Bedon C, Louter C. Numerical analysis of glass-FRP post-tensioned beams – Review and assessment.
791 *Compos Struct* 2017;177:129–40. <https://doi.org/10.1016/j.compstruct.2017.06.060>.
- 792 [23] Bedon C, Louter C. Finite Element analysis of post-tensioned SG-laminated glass beams with adhesively
793 bonded steel tendons. *Compos Struct* 2017;167:238–50.
794 <https://doi.org/10.1016/j.compstruct.2017.01.086>.
- 795 [24] Bedon C, Louter C. Finite-Element Numerical Simulation of the Bending Performance of Post-Tensioned
796 Structural Glass Beams with Adhesively Bonded CFRP Tendons. *Am J Eng Appl Sci* 2016;9(3):680–91.
797 <https://doi.org/10.3844/ajeassp.2016.680.691>.
- 798 [25] Louter C, Graaf A, Rots J. Modeling the Structural Response of Reinforced Glass Beams using an SLA
799 Scheme. In: Bos, Louter, Veer, editors. *Challenging Glas. 2 - Conf. Archit. Struct. Appl. Glas., Delft:*
800 2010.
- 801 [26] Bedon C, Louter C. Finite-element analysis of post-tensioned SG-laminated glass beams with
802 mechanically anchored tendons. *Glas Struct Eng* 2016;1:39–59. [https://doi.org/10.1007/s40940-016-0020-](https://doi.org/10.1007/s40940-016-0020-7)
803 7.
- 804 [27] Sena-Cruz J, Barros J, Azevedo A, Ventura-Gouveia A. Numerical Simulation of the Nonlinear Behavior
805 of RC Beams Strengthened With NSM CFRP Strips. C. 2007 - Congr. Numer. Methods Eng. XXVIII
806 CILAMCE - Iber. Latin-American Congr. Comput. Methods Eng., Porto: 2007, p. 13–5.
- 807 [28] Simulia. ABAQUS computer software and Online Documentation. v6.12. 2012.
- 808 [29] Yankelevsky DZ. Strength prediction of annealed glass plates - A new model. *Eng Struct* 2014;79:244–
809 55. <https://doi.org/10.1016/j.engstruct.2014.08.017>.
- 810 [30] Veer FA, Rodichev YM. The structural strength of glass: Hidden damage. *Strength Mater* 2011;43:302–
811 15. <https://doi.org/10.1007/s11223-011-9298-5>.
- 812 [31] Yankelevsky DZ. Size effect of the modulus of rupture in float glass plates. *Structures* 2020;27:1637–45.
813 <https://doi.org/10.1016/j.istruc.2020.08.006>.
- 814 [32] Rots J, Blaauwendraad J. Cracks Models for Concrete: Discrete or Smeared? Fixed, Multi-directional or
815 Rotating? *Heron* 1989;34.
- 816 [33] Bazant Z, Oh B. Crack band theory of concrete. *Mater Struct* 1983;16:155–77.
817 <https://doi.org/10.1007/BF02486267>.
- 818 [34] Sena-Cruz J. Strengthening of concrete structures with near-surface mounted CFRP laminate strips. Minho
819 University, 2005.
- 820 [35] Rots J, Nauta P, Kusters G, Blaauwendraad J. Smeared Crack Approach and Fracture Localization in
821 Concrete. *Heron* 1985;30.
- 822 [36] de Borst R. Computational methods in non-linear solid mechanics. Part 2: physical non-linearity.
823 Netherlands: 1991.
- 824 [37] Feldmann M, Kasper R. Guidance for European Structural Design of Glass Components. Luxembourg:
825 2014. <https://doi.org/10.2788/5523>.
- 826 [38] Mostafawi H. Experimental and Numerical Analysis of the Shear Ring. Royal Institute of Technology,
827 2014. <https://doi.org/10.1007/s00603-014-0560-6>.
- 828 [39] Chen G, Teng J, Chen J, Xiao Q. Finite element modeling of debonding failures in FRP-strengthened RC
829 beams : a dynamic approach. *Comput Struct* 2015;158:167–83.
830 <https://doi.org/10.1016/j.compstruc.2015.05.023>.
- 831 [40] López-Almansa F, Alfarah B, Oller S. Numerical simulation of RC frame testing with damaged plasticity
832 model comparison with simplified models. 2nd Eur. Conf. Earthq. Eng. Seismol., Istanbul: 2014, p. 1–12.
833 <https://doi.org/10.13140/2.1.3457.2169>.
- 834 [41] Coronado C, Lopez M. Sensitivity analysis of reinforced concrete beams strengthened with FRP laminates.
835 *Cem Concr Compos* 2006;28:102–14. <https://doi.org/10.1016/j.cemconcomp.2005.07.005>.
- 836 [42] Tao Y, Chen J. Concrete Damage Plasticity Model for Modeling FRP-to-Concrete Bond Behavior. *J*

- 837 Compos Constr 2015;19. [https://doi.org/10.1061/\(ASCE\)CC.1943-5614.0000482](https://doi.org/10.1061/(ASCE)CC.1943-5614.0000482).
838 [43] Kozłowski M, Kadela M, Hulimka J. Numerical Investigation of Structural Behaviour of Timber-Glass
839 Composite Beams. *Procedia Eng* 2016;161:990–1000. <https://doi.org/10.1016/j.proeng.2016.08.838>.
840 [44] Haldimann M, Luible A, Overend M. Structural use of glass. LABSE - Lanka Association of Building
841 Services Engineers; 2008.
842 [45] Jirásek M. Damage and smeared crack models. *CISM Int Cent Mech Sci Courses Lect* 2011;532:1–49.
843 https://doi.org/10.1007/978-3-7091-0897-0_1.
844 [46] Malm R. Shear cracks in concrete structures subjected to in-plane stresses. *Trita-Bkn Bull* 2006:136.
845 [https://doi.org/10.1016/S0009-2614\(00\)00726-0](https://doi.org/10.1016/S0009-2614(00)00726-0).
846

847 **LIST OF TABLES**

848	Table 1: Mechanical properties used to simulate the polyurethane adhesive using the bilinear bond-slip relationship
849	(<i>NLB</i> strategy).
850	Table 2: Mechanical properties used in [19] to describe the polyurethane adhesive joint of the <i>SFlex</i> beam.
851	Table 3: Elastic properties of the <i>SDur</i> and <i>SFlex</i> beams defined from the experimental and numerical responses,
852	as well as the difference of the numerically obtained properties in relation to the respective experimental
853	values.
854	Table 4: Mechanical properties of the elastic behaviour of <i>SDur</i> beams analytically calculated.
855	Table 5: Comparison between numerical and experimental axial strains in glass (SG1) and GFRP (SG4)
856	corresponding to F_{ck} and F_{ul} , and relative differences (in brackets) between numerical and experimental
857	strain values.
858	

859 **Table 1:** Mechanical properties used to simulate the polyurethane adhesive using the bilinear bond-slip
 860 relationship (NLB strategy).

K_n [MPa/mm]	K_t [MPa/mm]	τ_m [MPa]	G_m [N/mm]
10^6	0.4048	1.70	3.50

861

862 **Table 2:** Mechanical properties used in [19] to describe the polyurethane adhesive joint of the *SFlex* beam.

K_n [N/m ³]	τ_m [MPa]	s_m [mm]	α [-]	α' [-]
10^6	1.70	4.20	0.90	3.00

863

Table 3: Elastic properties of the *SDur* and *SFlex* beams defined from the experimental and numerical responses, as well as the difference of the numerically obtained properties in relation to the respective experimental values.

	<i>SDur</i> beams			<i>SFlex</i> beams		
	K_{el} [kN/mm]	F_{cr} [kN]	u_{ck} [mm]	K_{el} [kN/mm]	F_{cr} [kN]	u_{ck} [mm]
<i>SDur</i> -1	1.63	6.28	3.85	-	-	-
<i>SDur</i> -2	1.70	5.45	3.20	-	-	-
<i>SFlex</i> -1	-	-	-	1.55	3.80	2.45
<i>SFlex</i> -2	-	-	-	1.66	4.60	2.77
SCM-FEMIX	1.57 (-5.7%)	5.02 (-14.4%)	3.20 (-9.2%)	1.38 (-14.0%)	4.40 (4.8%)	3.18 (21.8%)
SCM-ABAQUS	1.55 (-6.9%)	5.04 (-14.1%)	3.25 (-7.8%)	1.41 (-12.1%)	4.76 (13.3%)	3.33 (27.6%)
DPM-ABAQUS	1.56 (-6.3%)	5.11 (-12.9%)	3.27 (-7.2%)	1.43 (-10.9%)	4.79 (14.0%)	3.36 (28.7%)

867 **Table 4:** Mechanical properties of the elastic behaviour of *SDur* beams analytically calculated.

$K_{el,a}$ [kN/mm]	$F_{ck,a}$ [kN]	$\delta_{ck,a}$ [mm]
1.590	4.897	3.080

868

Table 5: Comparison between numerical and experimental axial strains in glass (SG1) and GFRP (SG4) corresponding to F_{ck} and F_{ul} , and relative differences (in brackets) between numerical and experimental strain values.

	F = F_{cr}		F = F_{ul}	
	SG1 [‰]	SG4 [‰]	SG1 [‰]	SG4 [‰]
<i>SFlex-1</i> (Exp.)	-0.53	0.20	-0.24	2.20
SCM-FEMIX	-0.59 (10.9%)	0.24 (20.1%)	-0.26 (7.9%)	1.76 (-19.2%)
SCM-ABAQUS	-0.57 (7.2%)	0.22 (15.5%)	-0.24 (-1.2%)	1.67 (-23.5%)
DPM-ABAQUS	-0.57 (7.2%)	0.22 (12.8%)	-0.25 (4.4%)	1.56 (-28.6%)

873 LIST OF FIGURES

- 874 Fig. 1. Four-point bending tests of the glass-GFRP composite beams: (a) schematic representation;
875 (b) experimental setup [19]. Note: units in [mm].
- 876 Fig. 2. Load *vs.* relative displacement obtained from tensile tests on double-lap joints with polyurethane (a) and
877 epoxy (b) adhesives [19].
- 878 Fig. 3. Structural responses (load *vs.* deflection) obtained from the experimental tests: (a) *SDur* beams; (b) *SFlex*
879 beams [19].
- 880 Fig. 4. Experimental crack patterns: (a) *SDur* beams; (b) *SFlex* beams [19].
- 881 Fig. 5. Axial strains *vs.* load measured at different depths of the *SFlex*-1 beam mid-span section.
- 882 Fig. 6. Damage law adopted for simulating glass behaviour.
- 883 Fig. 7. Load *vs.* deflection curves of the *SDur* and *SFlex* beams obtained from the SCM-FEMIX, and
884 corresponding crack pattern at different phases, (i), (ii), (iii) and (iv).
- 885 Fig. 8. Load *vs.* deflection curves of the *SDur* and *SFlex* beams obtained from the SCM-ABAQUS, and
886 corresponding crack pattern at different phases, (i), (ii), (iii) and (iv).
- 887 Fig. 9. Load *vs.* deflection curves of the *SDur* and *SFlex* beams obtained from the DPM-ABAQUS, and
888 corresponding crack pattern at different phases, (i), (ii), (iii) and (iv).
- 889 Fig. 10. Load *vs.* deflection curves obtained from the experimental tests and distinct numerical models: (a) *SDur*
890 beams; (b) *SFlex* beams.
- 891 Fig. 11. Ratio between the slope of the load *vs.* deflection curves and the elastic stiffness for the *SDur* beams
892 obtained from the ABAQUS models.
- 893 Fig. 12. Ratio E_v/E_w along the tangent line of the load *vs.* displacement curves of the DPM-ABAQUS.
- 894 Fig. 13. Load *vs.* deflection curves of the *SDur* beams obtained from SCM-FEMIX and SCM-FEMIX 90°, and
895 corresponding crack pattern at different phases, (i), (ii), (iii), (iv), (v) and (vi).
- 896 Fig. 14. Load *vs.* displacement curves of *SDur* beams obtained from the three initial material models and the SCM-
897 FEMIX 90°.
- 898 Fig. 15. Sensitivity of both ABAQUS material models in relation to the mesh pattern.
- 899 Fig. 16. Sensitivity of both ABAQUS model in relation to the fracture energy.
- 900 Fig. 17. Sensitivity of DPM-ABAQUS in relation to the dilation angle.
- 901 Fig. 18. Sensitivity of DPM-ABAQUS in relation to the shape of the yield surface.
- 902 Fig. 19. E_k/E_t ratio along the load *vs.* deflection curves of the SCM-ABAQUS (a) and DPM-ABAQUS (b).
- 903 Fig. 20. Load *vs.* deflection curves of the *SFlex* beams obtained from SCM-FEMIX and SCM-FEMIX-A, and
904 corresponding crack pattern at different phases, (i) and (ii).
- 905 Fig. 21. Load *vs.* deflection curves of the *SFlex* beams obtained from the three material models and the SCM-
906 FEMIX A.
- 907 Fig. 22. Elastic stiffness *vs.* deflection diagrams of the *SFlex* beams.
- 908 Fig. 23. Load *vs.* deflection curves of the *SFlex* beams obtained from SCM-FEMIX and SCM-FEMIX A/90°, and
909 corresponding crack pattern at different phases, (i) and (ii).
- 910 Fig. 24. Load *vs.* deflection curves of the *SFlex* beams obtained from the three material models and the SCM-
911 FEMIX A/90°.
- 912 Fig. 25. Comparison between numerical and experimental axial strains at the mid-span section of the *SFlex*-1 beam
913 corresponding to (a) the cracking load F_{ck} and (b) the ultimate load F_{ul} .
- 914 Fig. 26. Localized bending effect at the GFRP reinforcement caused by the formation and propagation of a crack
915 in the glass pane (in the vicinity).
- 916 Fig. 27. E_k/E_t ratio along the load *vs.* deflection curves of the SCM-ABAQUS (a) and DPM-ABAQUS (b).
917

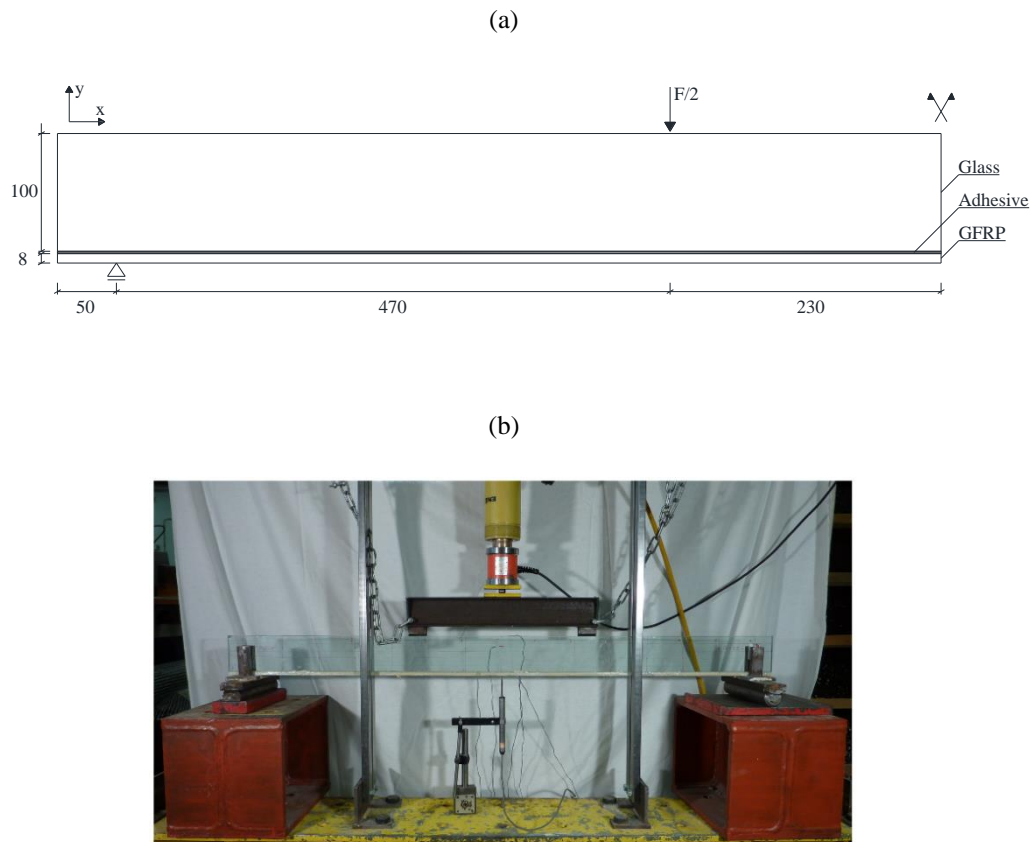


Fig. 1. Four-point bending tests of the glass-GFRP composite beams: (a) schematic representation; (b) experimental setup [19]. Note: units in [mm].

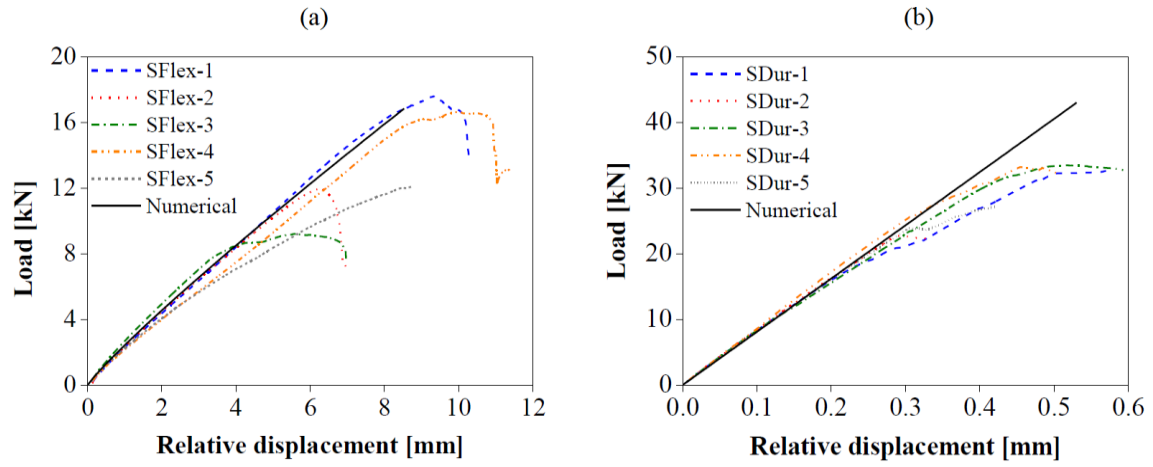


Fig. 2. Load vs. relative displacement obtained from tensile tests on double-lap joints with polyurethane (a) and epoxy (b) adhesives [19].

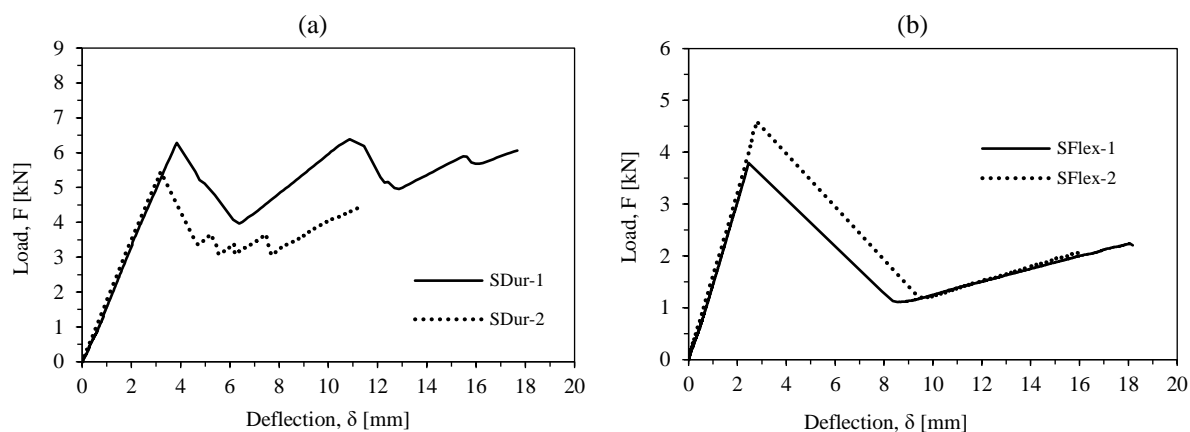


Fig. 3. Structural responses (load vs. deflection) obtained from the experimental tests: (a) *SDur* beams; (b) *SFlex* beams [19].

(a)



(b)



927 **Fig. 4.** Experimental crack patterns: (a) *SDur* beams; (b) *SFlex* beams [19].

928

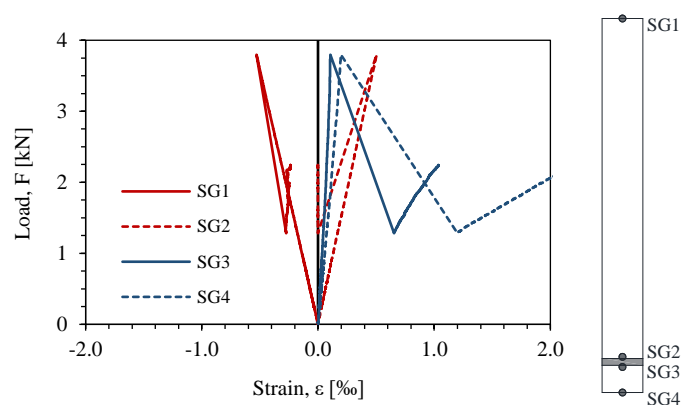


Fig. 5. Axial strains vs. load measured at different depths of the *SFlex-1* beam mid-span section.

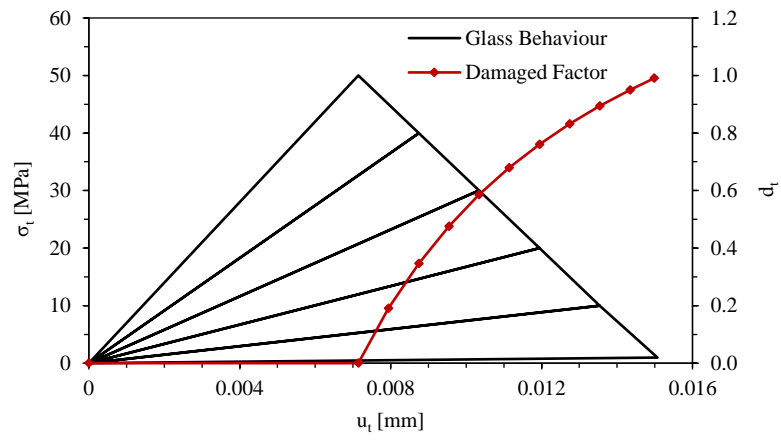


Fig. 6. Damage law adopted for simulating glass behaviour.

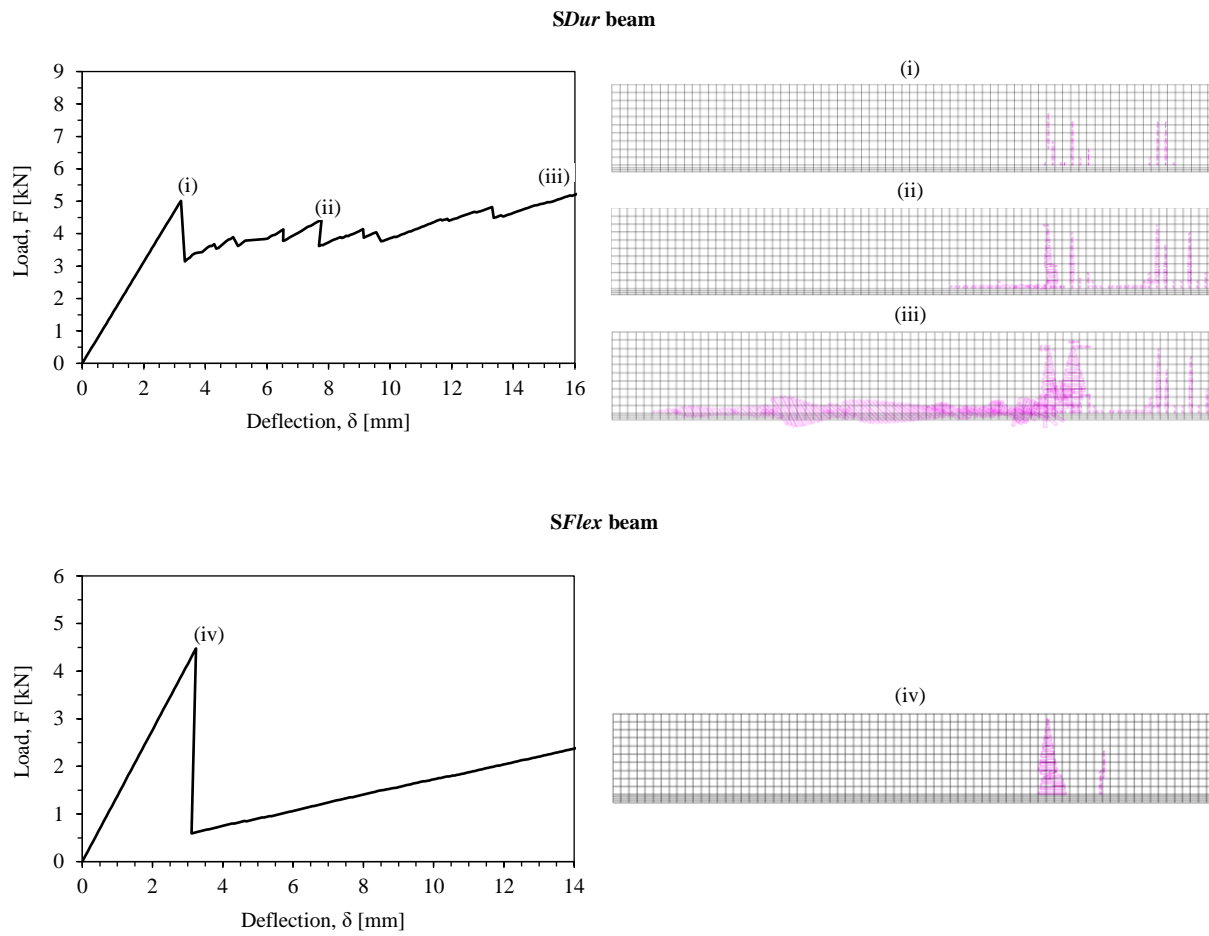


Fig. 7. Load vs. deflection curves of the *SDur* and *SFlex* beams obtained from the SCM-FEMIX, and corresponding crack pattern at different phases, (i), (ii), (iii) and (iv).

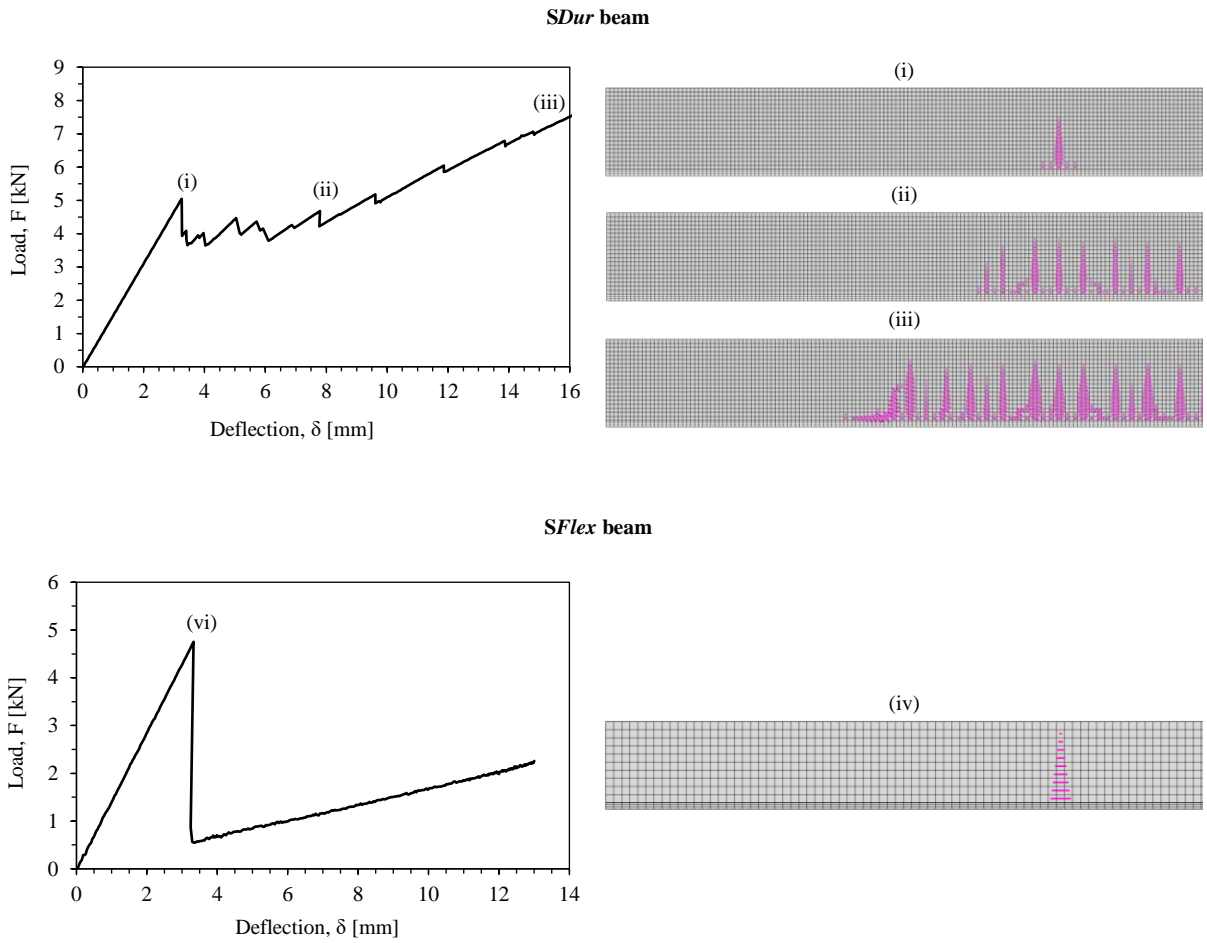


Fig. 8. Load vs. deflection curves of the *SDur* and *SFlex* beams obtained from the SCM-ABAQUS, and corresponding crack pattern at different phases, (i), (ii), (iii) and (iv).

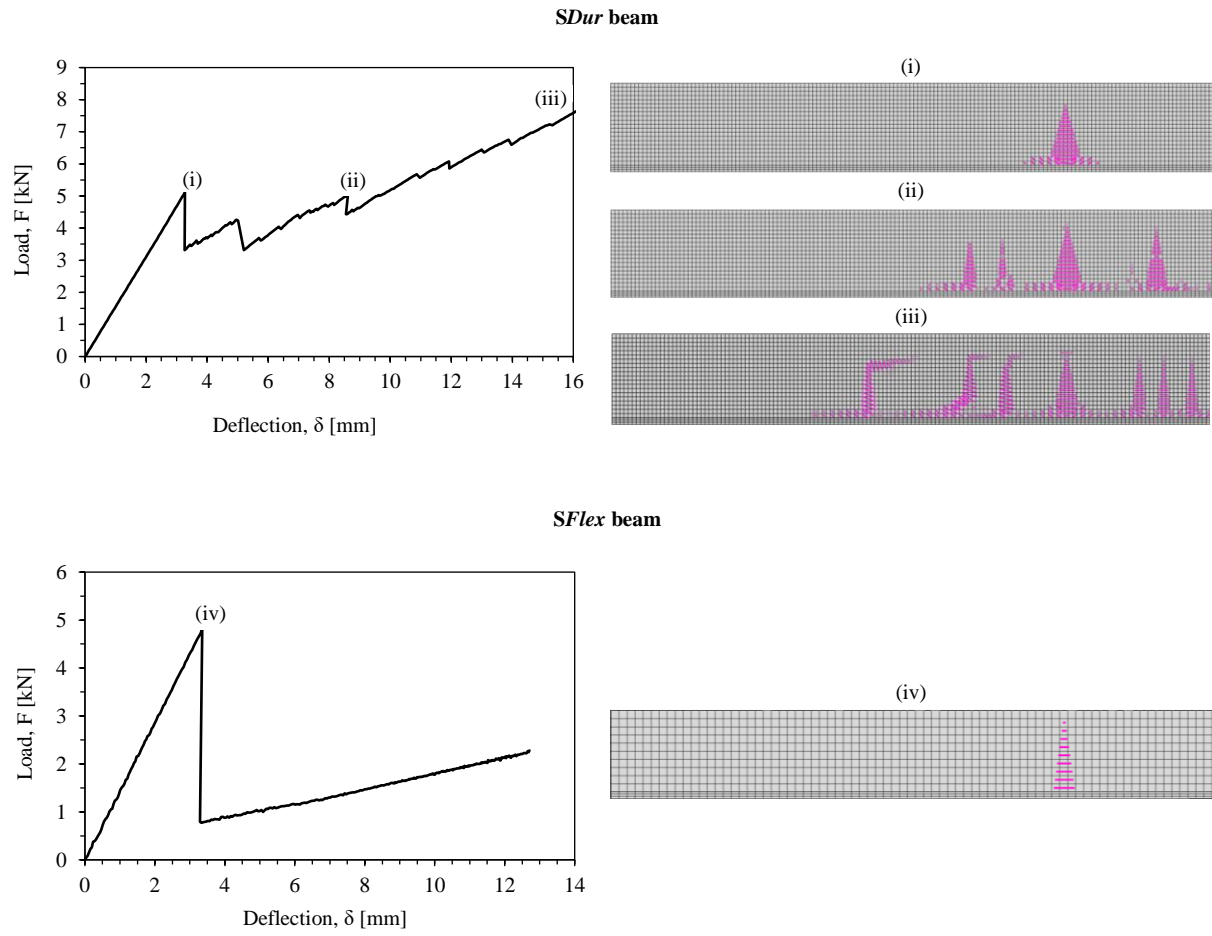


Fig. 9. Load vs. deflection curves of the *SDur* and *SFlex* beams obtained from the DPM-ABAQUS, and corresponding crack pattern at different phases, (i), (ii), (iii) and (iv).

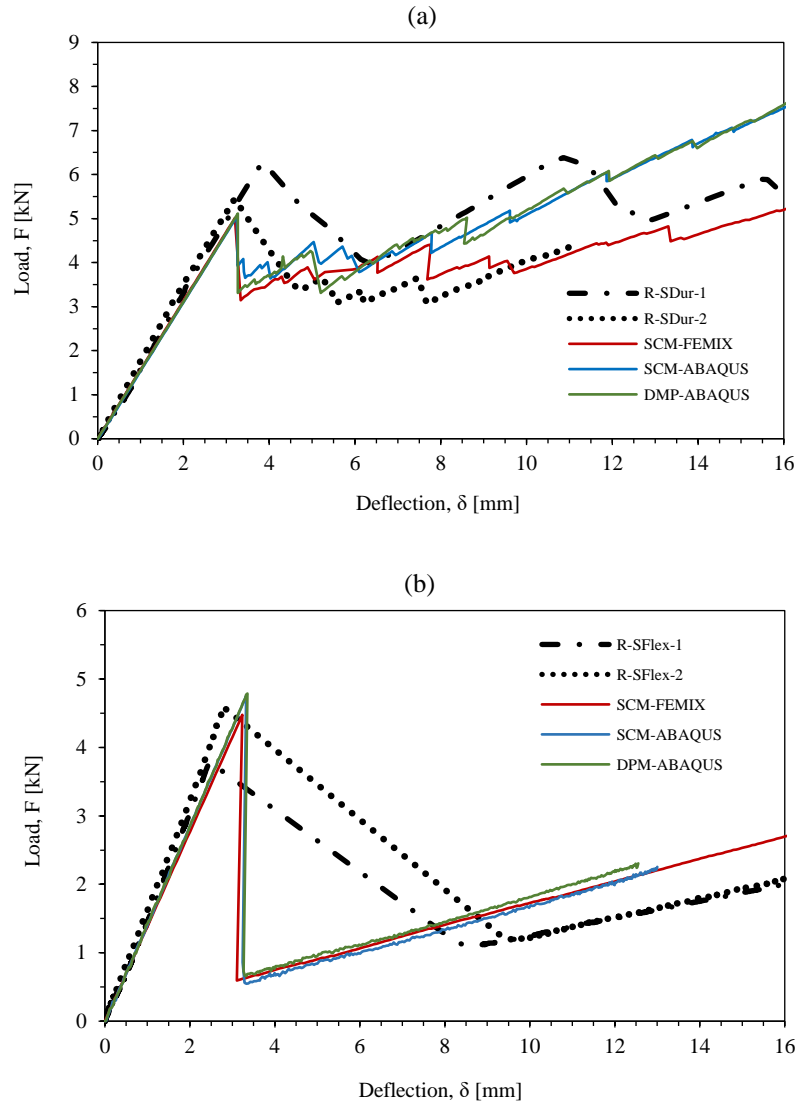


Fig. 10. Load vs. deflection curves obtained from the experimental tests and distinct numerical models: (a) *SDur* beams; (b) *SFlex* beams.

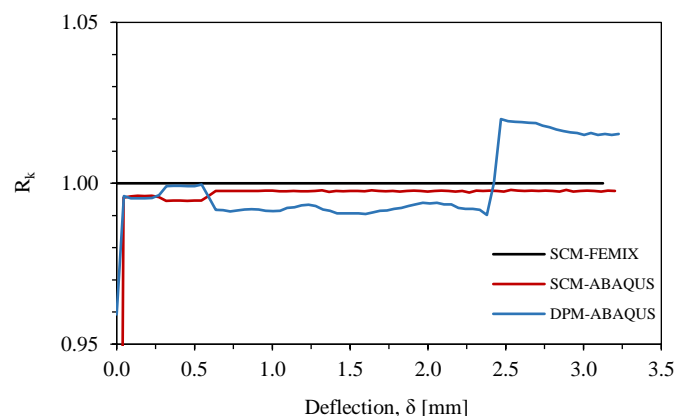


Fig. 11. Ratio between the slope of the load vs. deflection curves and the elastic stiffness for the *SDur* beams obtained from the ABAQUS models.

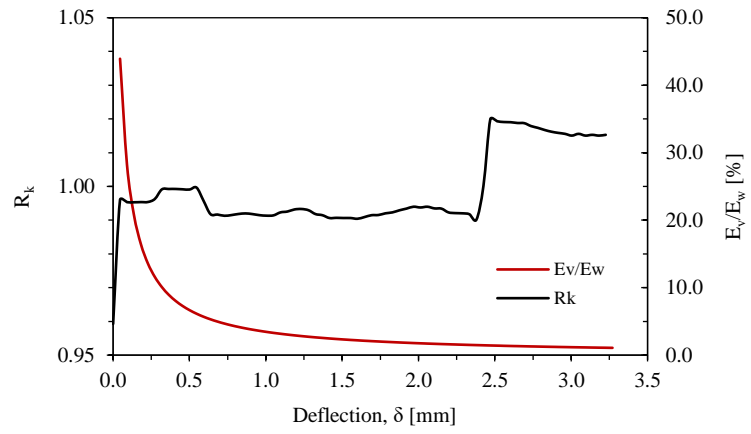


Fig. 12. Ratio E_v/E_w along the tangent line of the load vs. displacement curves of the DPM-ABAQUS.

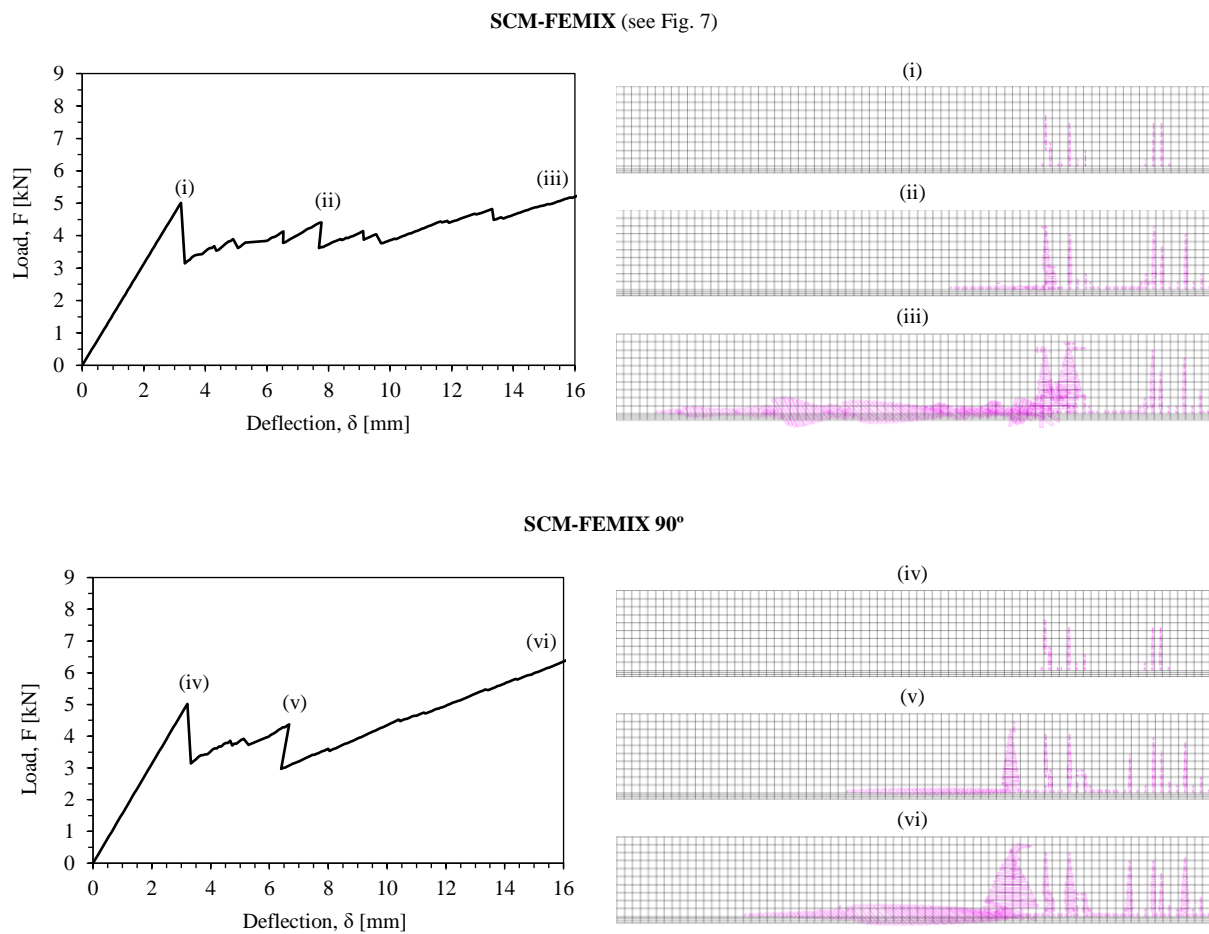


Fig. 13. Load vs. deflection curves of the *SDur* beams obtained from SCM-FEMIX and SCM-FEMIX 90°, and corresponding crack pattern at different phases, (i), (ii), (iii), (iv), (v) and (vi).

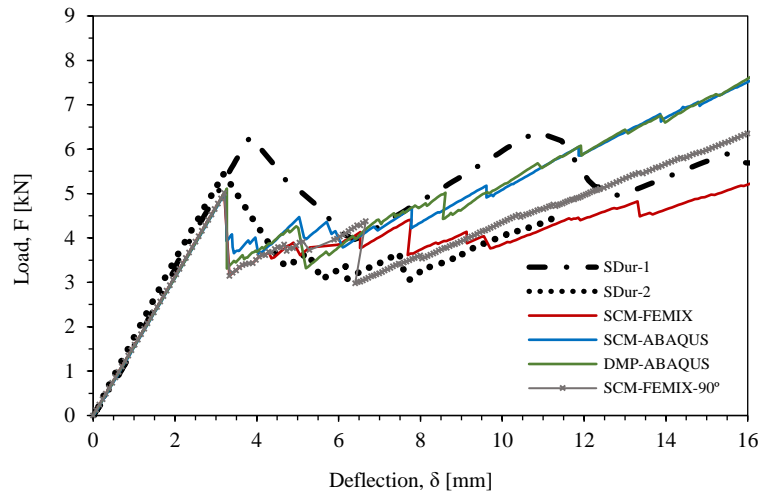


Fig. 14. Load vs. displacement curves of *SDur* beams obtained from the three initial material models and the SCM-FEMIX 90°.

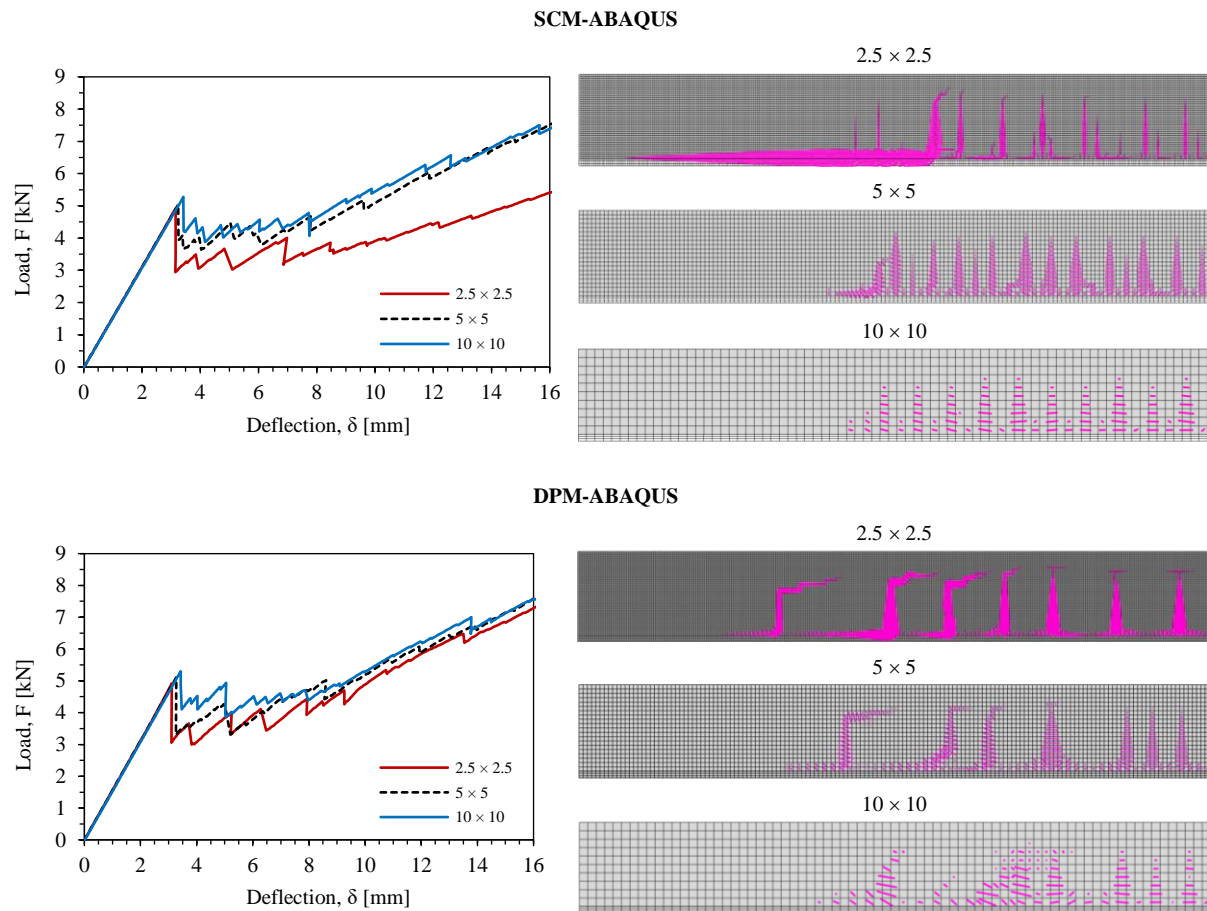
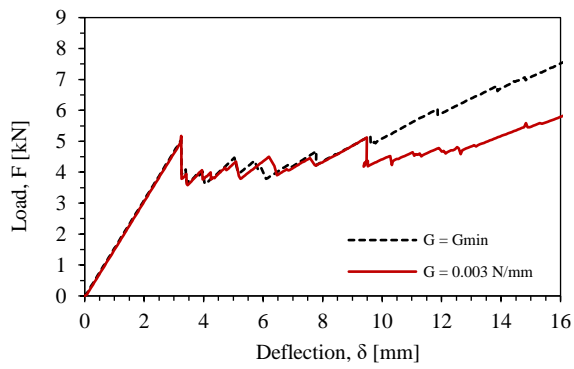
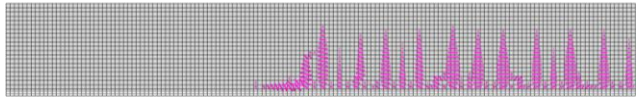


Fig. 15. Sensitivity of both ABAQUS material models in relation to the mesh pattern.

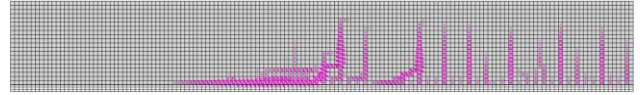
SCM-ABAQUS



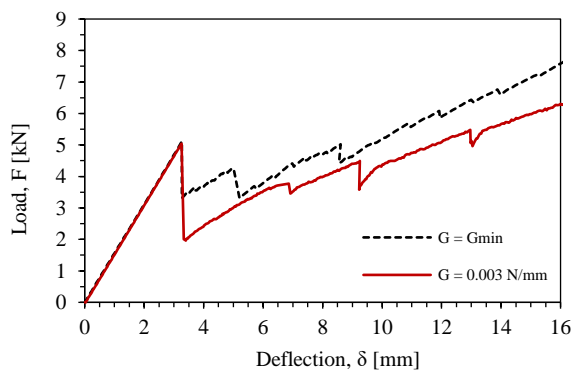
G = Gmin



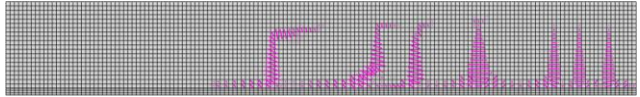
G = 0.003 N/mm



DPM-ABAQUS



G = Gmin



G = 0.003 N/mm



Fig. 16. Sensitivity of both ABAQUS model in relation to the fracture energy.

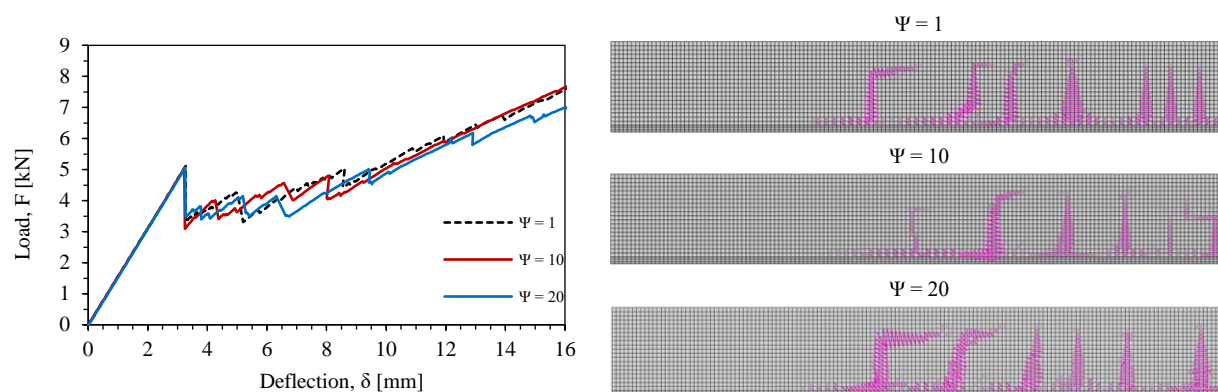


Fig. 17. Sensitivity of DPM-ABAQUS in relation to the dilation angle.

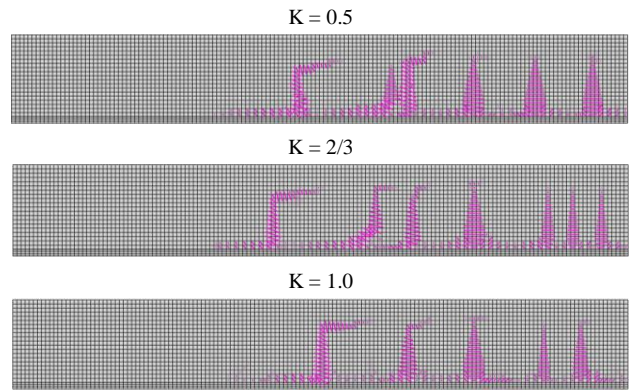
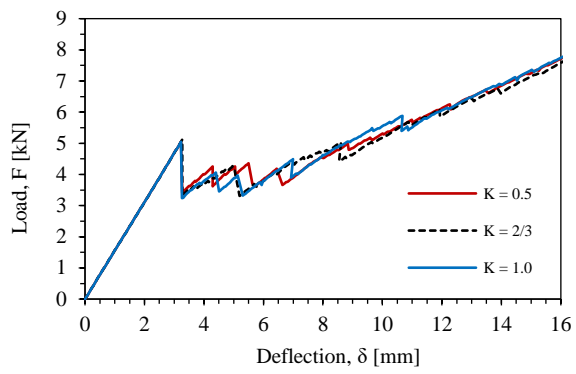


Fig. 18. Sensitivity of DPM-ABAQUS in relation to the shape of the yield surface.

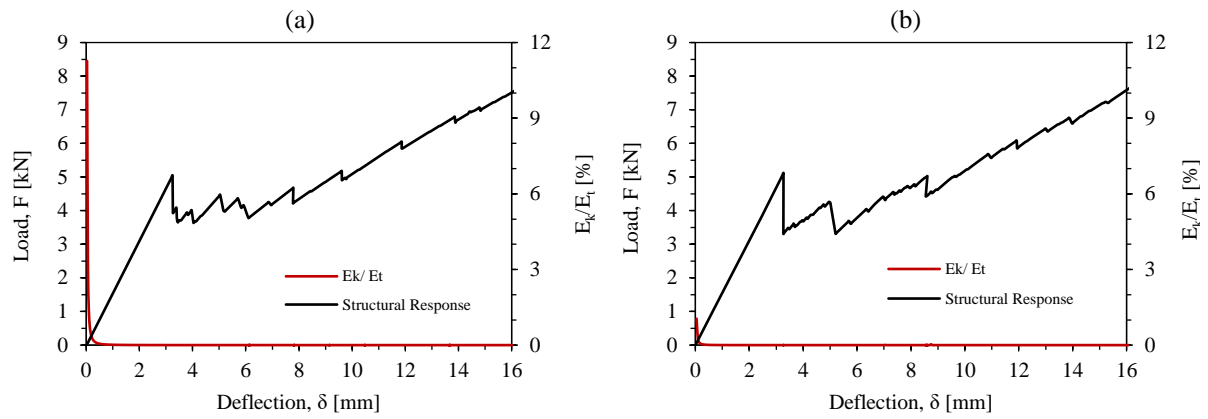
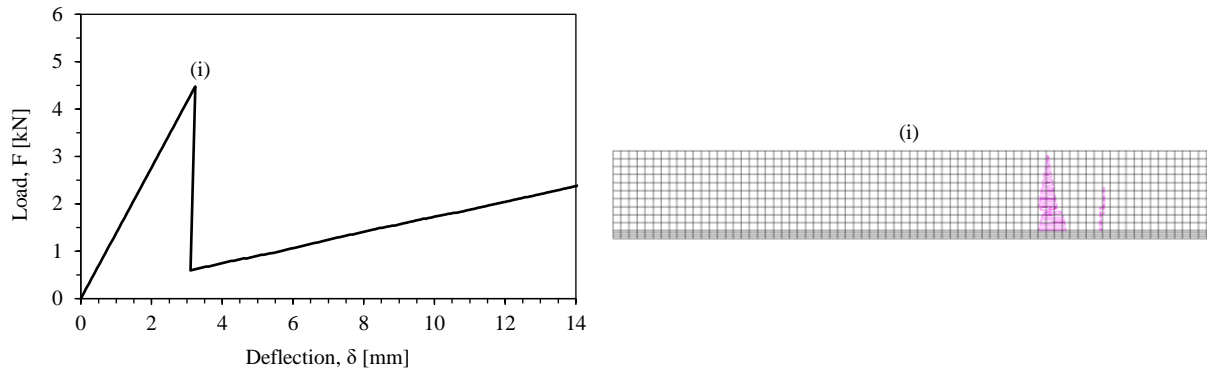


Fig. 19. E_k/E_t ratio along the load vs. deflection curves of the SCM-ABAQUS (a) and DPM-ABAQUS (b).

SCM-FEMIX (see Fig. 7)



SCM-FEMIX-A

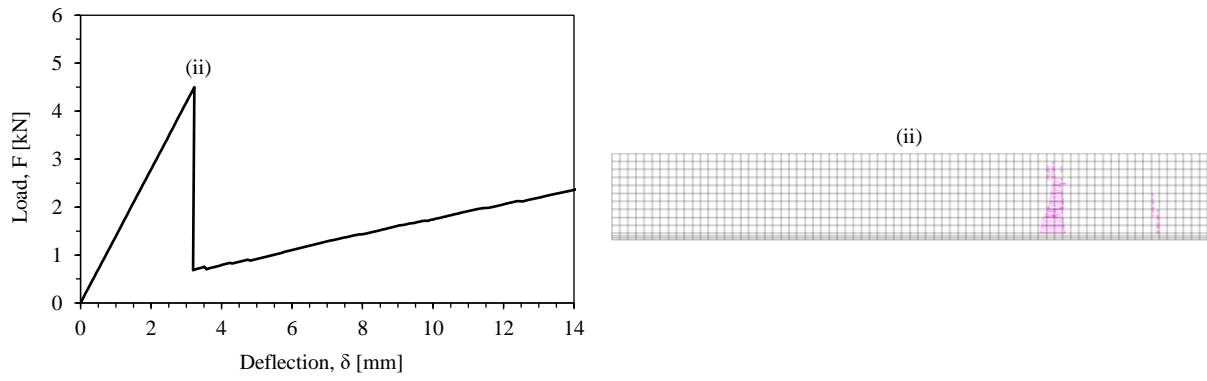


Fig. 20. Load vs. deflection curves of the *SFlex* beams obtained from SCM-FEMIX and SCM-FEMIX-A, and corresponding crack pattern at different phases, (i) and (ii).

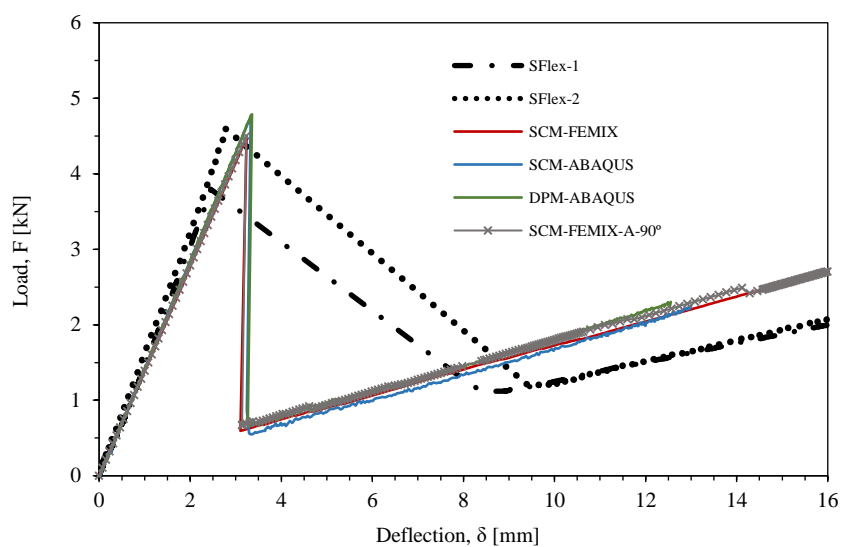


Fig. 21. Load vs. deflection curves of the *SFlex* beams obtained from the three material models and the SCM-FEMIX A.

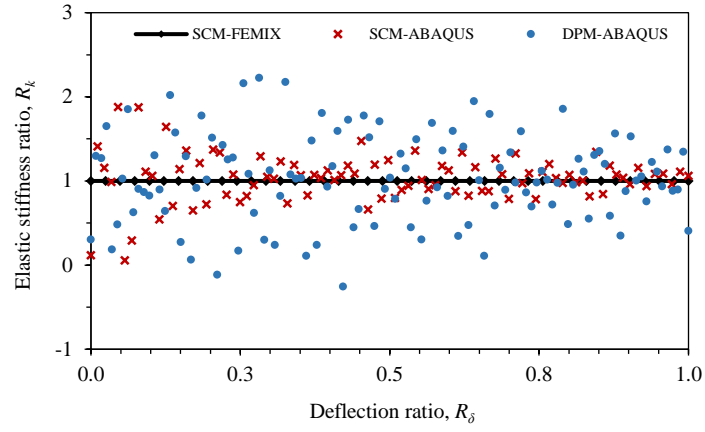


Fig. 22. Elastic stiffness vs. deflection diagrams of the *SFlex* beams.

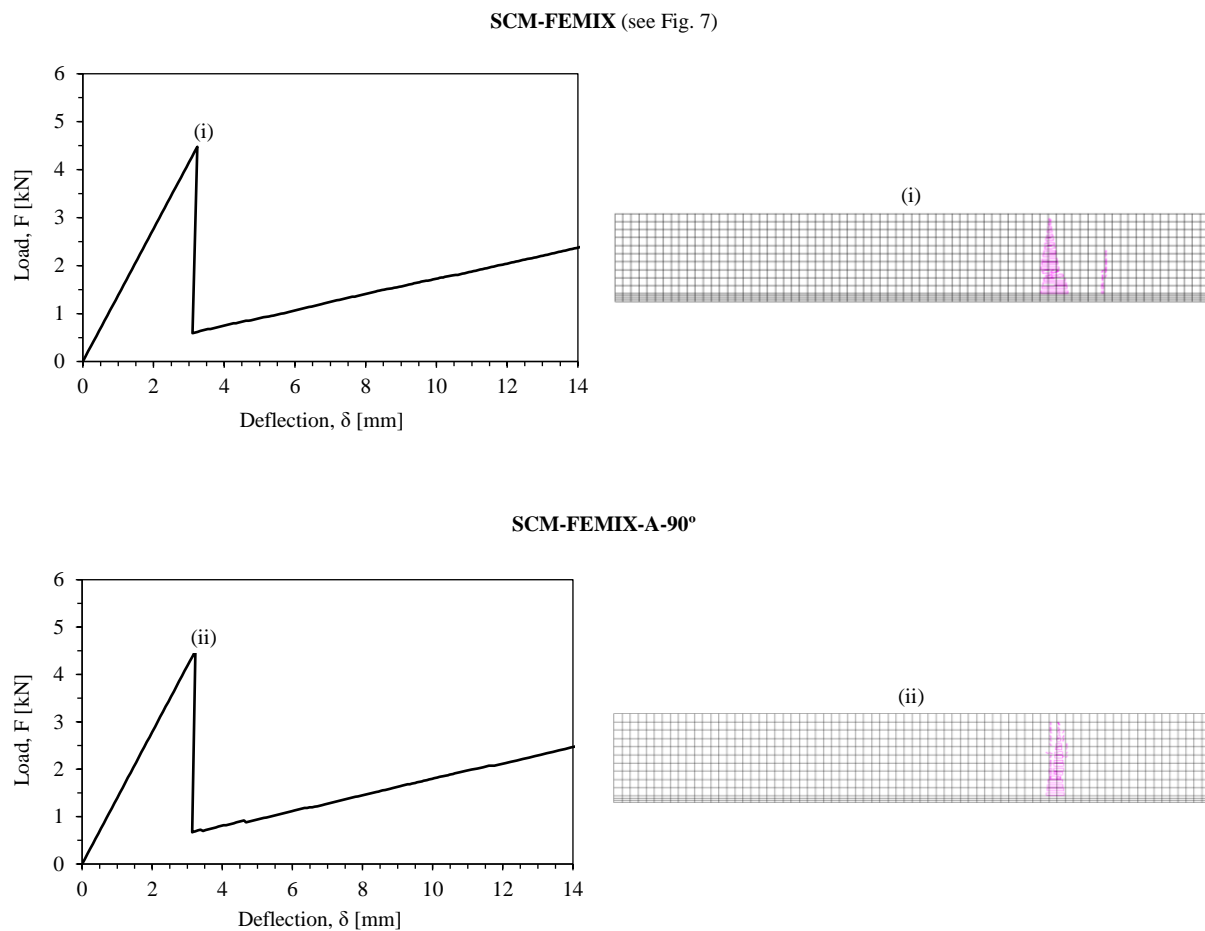


Fig. 23. Load vs. deflection curves of the *SFlex* beams obtained from SCM-FEMIX and SCM-FEMIX A/90°, and corresponding crack pattern at different phases, (i) and (ii).

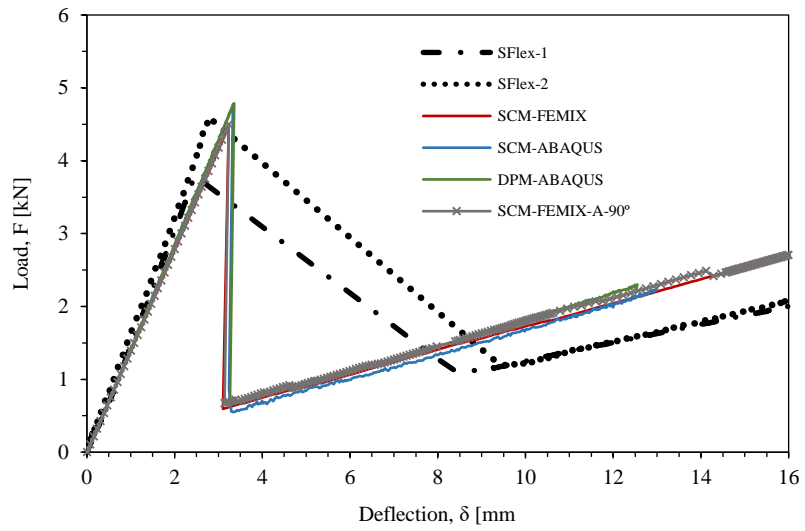


Fig. 24. Load vs. deflection curves of the *SFlex* beams obtained from the three material models and the SCM-FEMIX A/90°.

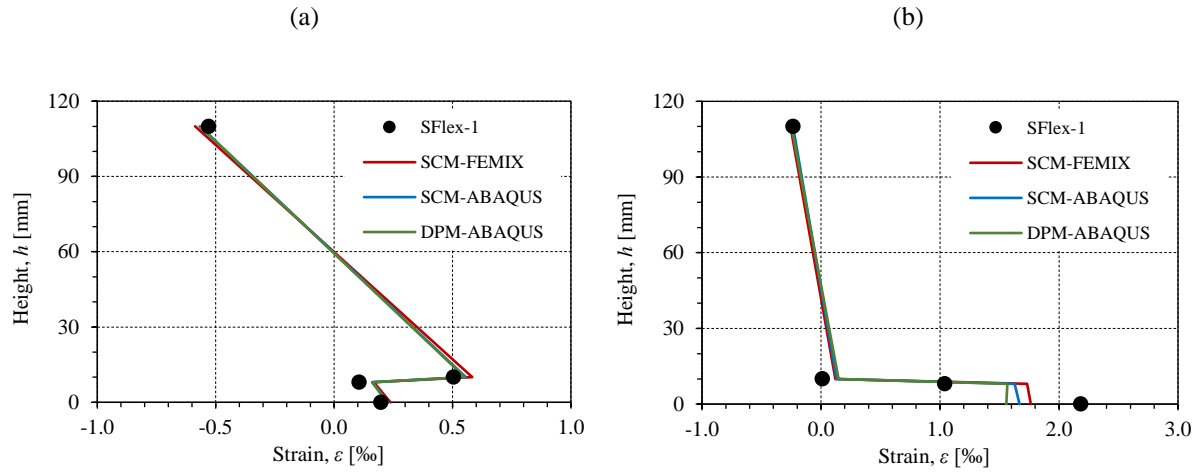


Fig. 25. Comparison between numerical and experimental axial strains at the mid-span section of the *SFlex-1* beam corresponding to (a) the cracking load F_{ck} and (b) the ultimate load F_{ul} .

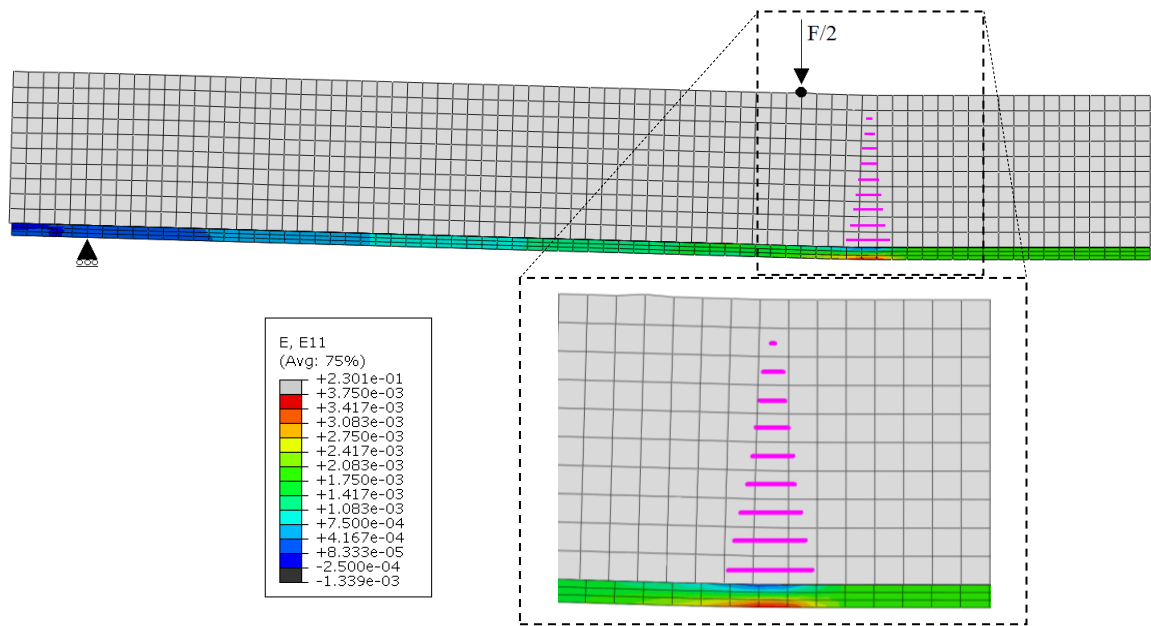
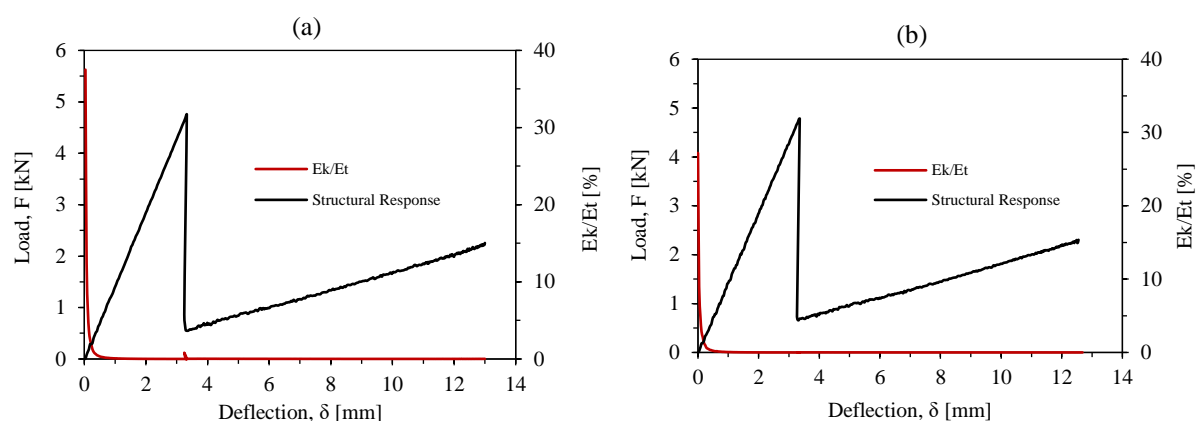


Fig. 26. Localized bending effect at the GFRP reinforcement caused by the formation and propagation of a crack in the glass pane (in the vicinity).



986 **Fig. 27.** E_k/E_t ratio along the load vs. deflection curves of the SCM-ABAQUS (a) and DPM-ABAQUS (b).